Bimetallic Au-Ag Nanorod Dimers as Plasmonic Biosensors

A Thesis
Submitted to the Department of Electrical and Electronics Engineering,
BRAC University

Supervisor**:**

Avijit Das

Submitted by**:**

Md Ahnaf Rahman- ID: 12221114

Aishik Hossain - ID: 13321014

Mohammed Shadman Hossain- ID: 12221094

In partial fulfillment of the requirements for the degree of Bachelor of Science in Electrical and Electronic Engineering
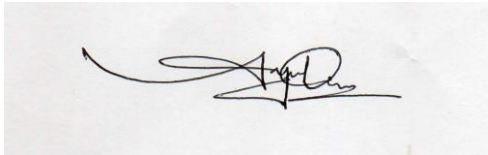
Summer 2017
BRAC University, Dhaka

Declaration

We, hereby, declare that this thesis is based on self-derived results. Materials that support our work by other researchers are mentioned in the reference section. This Thesis, neither in whole nor in part, has been previously submitted for any degree.

Signature of the Supervisor: Signature of the authors:

_____   _____

Avijit Das   Aishik Hossain

                                                                                    _____

                                                                                    Md Ahnaf Rahman

                                                                                    _____

                                                                                    Mohammed Shadman Hossain

<u>Acknowledgement</u>

Abstract

Fano resonance, discovered by Italian-American physicist Ugo Fano, is a general wave phenomenon and is seen throughout many areas of engineering and physics. It is a kind of resonant scattering occurrence that results in an asymmetrical line shape. This unbalance is created due to interference between a resonant and a background scattering process. In the field of plasmonic nanostructures, Fano resonance has potential applications in bio-sensing and nonlinear optoelectronics. In this report, we study the Fano resonance in heterogeneous Au-Ag nanorod pairs (dimers). Finite Difference Time Domain (FDTD) method is used to solve Maxwell's equations and calculate the absorption, scattering, and electric field spectrum in both near-field and far-field regions. The consequent Fano line-shape can be used to sense biologically interesting molecules such as a protein or a cell. Further electrodynamics characterization and calculations show that the resonance originates from the interference of a narrow quadrupolar and a wide quadrupolar plasmon mode of a nanorod.

Table of Contents

Table of Figures

1. Introduction

The interaction between light and matter is central to life and to science. Sunlight is the primary source of all useful energy on the Earth. Most of us know what is in the world around us because of light that passes into our eyes. Our scientific understanding of the world has, for a large part, been based on extending our vision using optical instruments, from telescopes to see the very large to microscopes to see the very small. Our information economy is enabled by optical signals that travel down glass fibres. However, there are limits on our ability to put light to use. For a long time, it was thought that a fundamental limit was set by the wavelength of light itself. Propagating waves, whether they are light waves, radio waves, sound waves, or any other kind of wave, cannot be focused down to a spot smaller than about half their wavelength. For visible light, wavelengths range from about 400 to about 750 nm. This would seem to keep optics, at best, on the outskirts of nanoscience and nanotechnology. However, it has recently come to be understood that this is not always the case — that "Nano-optics" is not necessarily a contradiction.

1.1 Historical perspective

The tremendous amount of work now dedicated to plasmonic metal nanoparticles may give the impression that they are a recent discovery. In fact, they have a long and illustrious scientific and technological history, and the current excitement is more oaf revival of a long-standing interest. In a sense, people have been producing plasmonic metal nanoparticles for over1500 years. A red stained glass can be made by dissolving small quantity of gold compounds into the glass and then heating it in the presence of suitable chemical reducing agents. This results in the formation of gold nanoparticles inside the glass matrix. The nanoparticles have plasmon resonances at green wavelengths, so that light that passes through the glass looks red. The oldest known artefact based on this process is the Lycurgus cup, a glass vessel produced around 300 A.D. and now housed in the British Museum.

Figure 1 The Lycurgus Cup

The oldest written treatise on glass making, published in 1612 by Antonio Neri, describes how to stain glass red using gold. Of course, the glass stainers had no idea that they were producing gold nanoparticles, or that plasmon resonances were responsible for the red colours they were producing. The same is true for the production of colloidal gold, which dates back to the sixteenth century. Alchemists such as Paracelsus produced solutions of stably suspended gold nanoparticles with deep, red colours; the mysterious, blood-like colour of these solutions inspired a belief that they had powerful medicinal properties. Indeed, even now it is easy to find any number of quack vendors selling colloidal gold and silver as cure-all elixirs. (Silver solutions have historically had legitimate medical value as antimicrobial agents, but have the potential for adverse side effects, and have been replaced with more effective and safer antiseptics and antibiotics.) These solutions have also found less questionable use to stain glasses, ceramics, and fabrics. One such preparation was described in 1865 by Andreas Cassius, and is known as "purple of Cassius." It consists of a mixture of gold nanoparticles and colloidal stannic acid, and is made by dissolving gold in *aqua regia* and then precipitating it with a solution of tin in *aqua regia*.

1.2 Nano-plasmonics

When light is incident on a metal nanoparticle, its electric field pushes the electrons in the particle toward one side of the particle. This means that the negative charges of the electrons accumulate on that side, leaving behind a positive charge on the opposite side. These negative and positive charges attract one another; if the negative charge were suddenly released, then, it would oscillate back and forth with a certain frequency, like a mass on a spring. If the frequency of the incident light matches this natural resonance frequency, it will produce large oscillations of all of the free electrons in the metal. Because so many electrons are oscillating back and forth together, large electric fields are produced in the immediate vicinity of the particle; these fields themselves act on the electrons, reinforcing the oscillations. This coupled excitation, consisting of oscillating charges inside the particle and oscillating electromagnetic fields immediately outside the particle, is known as a plasmon resonance (or, often, as a localized surface plasmon or a particle plasmon).

1.3 Application of Surface Plasmon Resonance

This new, nanoscale control over light opens up unprecedented technological opportunities. To cite just a few examples, plasmon resonances in metal nanoparticles allow for highly sensitive chemical sensing and identification, own to the level of single molecules. Luminescence from molecules or semiconductor nanostructures can be enhanced by nearby metal nanoparticles, potentially enabling a new generation of light-emitting devices. The ability of metal nanoparticles to squeeze light down to nanoscale volumes provides unprecedented resolution for near-field optical microscopy, optical patterning, and optically assisted data storage. Metal nanoparticles can reduce the size, and thus increase the performance, of photodetectors, and may improve the efficiency of solar-energy conversion. Advanced materials composed of metal nanostructures can have the novel optical characteristics, such as negative refraction, required to realize exotic phenomena such as superlensing and optical cloaking. Metal nanoparticles with resonances in the near infrared can be functionalized to selectively attach to cancer cells; illumination of these nanoparticles with resonant light heats up the particles, eliminating tumours without damaging nearby tissue. Selective heating of metal nanoparticles is similarly being investigated for laser-assisted remote release of attached materials for targeted drug delivery. It is this seemingly

limitless promise of plasmonic metal nanoparticles that has inspired an explosion of research into the fabrication, characterization, and understanding of Plasmon resonances in metal nanostructures.

1.4 Application in Medical Sector of Surface Plasmon Resonance

The fields that have recently been greatly impacted by the advancement in nanostructured materials1 are biology, biophysics, and medicine. The nanobiology toolkit has been greatly enhanced by noble metal nanostructures, 2 which have proven to be highly versatile and tuneable materials for a range of bioapplications including biophysical studies, 3, 4 biological sensing, 5, 6 imaging, 7–9 medical diagnostics, 10 and cancer therapy.11–17
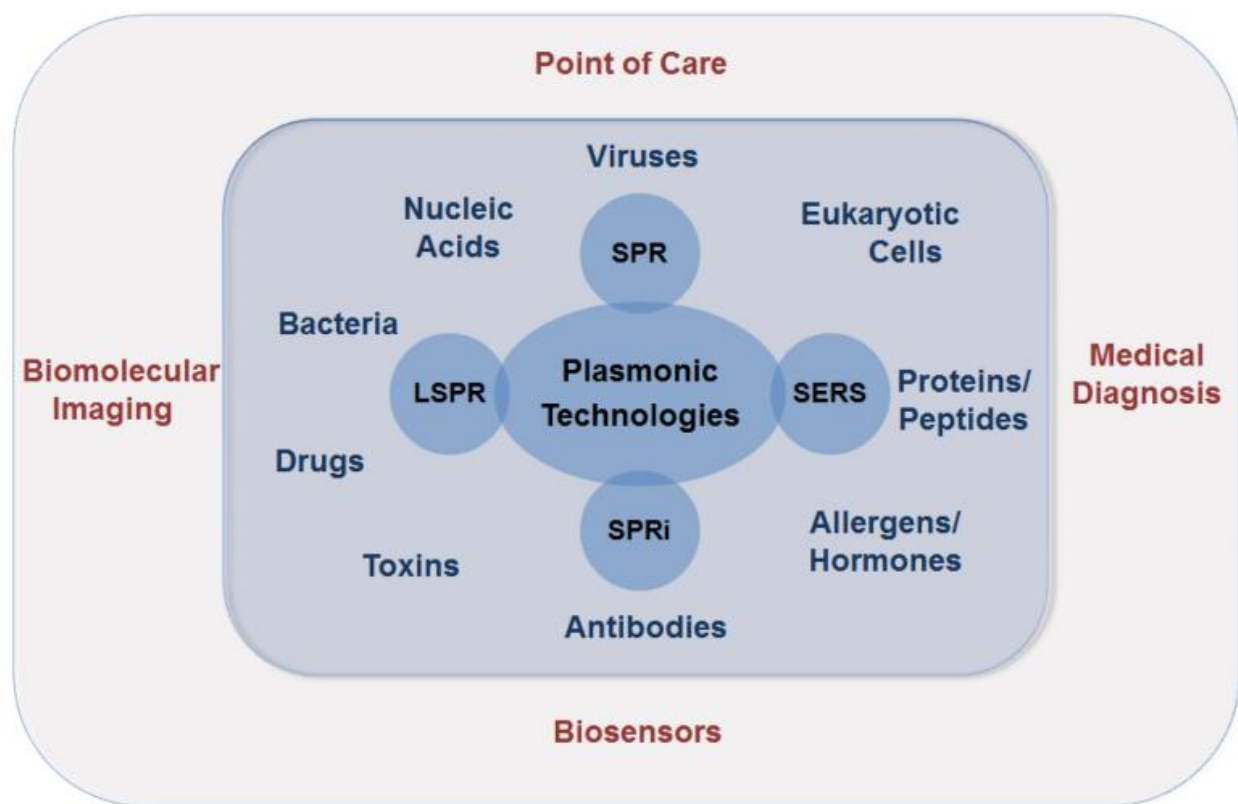
Figure 2 Different Plasmonic technologies and their respective applications

Metal nanoparticles serve as "light-activated nanoscopic heaters" useful for biomedicine, especially the selective laser photothermolysis of cancer cells. Gold nanoparticles conjugated to antibodies can be selectively targeted to cancer cells without significant binding to healthy cells.

Irradiation of the cancer cells selectively labelled with the nanoparticles with a laser of frequency overlapping with the LSPR absorption maximum of the nanoparticles results in selective heating and destruction of cancer cells at much lower laser powers than those required to destroy healthy cells to which nanoparticles do not bind specifically.
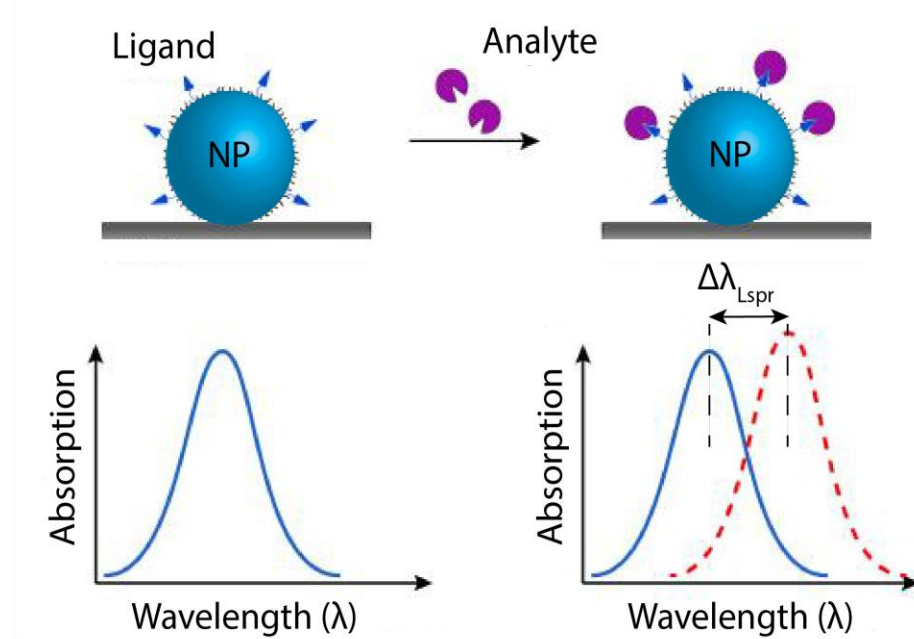
Figure 3 (Top) Binding of an analyte to a nanoparticle via a ligand. (Bottom) A redshift of the absorption spectrum is seen when an there is an increase in refractive index of the surrounding environment.

2. Physics behind LSPR

2.1 Surface plasmons

Surface plasmons, also known as surface plasmon polaritons, are surface electromagnetic waves that propagate in a direction parallel to the metal/dielectric (or metal/vacuum) interface. These are charge-density oscillations localized at the interface between a metallic film (active layer) and dielectric surface. Since the wave is on the boundary of the metal and the external medium (air or water for example), these oscillations are very sensitive to any change of this boundary, such as the adsorption of molecules to the metal surface.
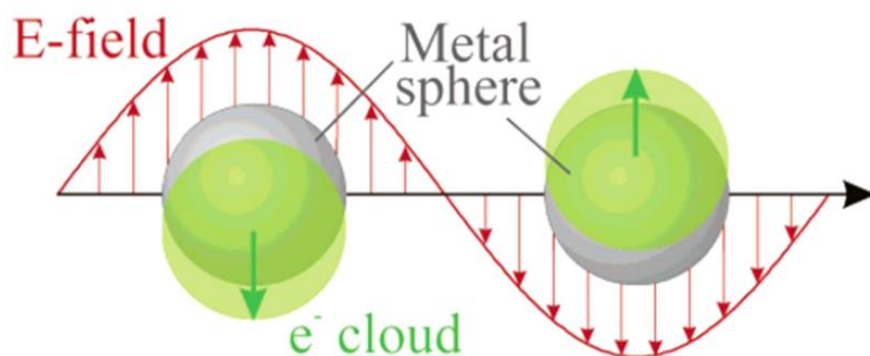
Figure 4 Schematic diagram of surface plasmon resonance

To describe the existence and properties of surface plasmons, one can choose from various models (quantum theory, Drude model, etc.). The simplest way to approach the problem is to treat each material as a homogeneous continuum, described by a frequency-dependent relative permittivity between the external medium and the surface. This quantity, hereafter referred to as the materials' "dielectric constant," is complexpermittivity. In order for the terms which describe the electronic surface plasmons to exist, the real part of the dielectric constant of the metal must be negative and its magnitude must be greater than that of the dielectric. This condition is met in the IR-visible wavelength region for air/metal and water/metal interfaces (where the real dielectric constant of a metal is negative and that of air or water is positive).

SPR can be described as the resonant, collective oscillation of valence electrons in a solid stimulated by incident light. The resonance condition is established when the frequency of light photons matches the natural frequency of surface electrons oscillating against the restoring force of positive nuclei. When planar surface is involved, then excitation of surface plasmon (Surface plasmons, also known as polaritons, are surface electromagnetic waves that propagate in a direction parallel to the metal/dielectric interface) by light is called SPR

2.2 LSPR

SPR in nanometer-sized structures is called *Localized surface plasmon resonance*. LSPRs are collective electron charge oscillations in metallic nanoparticles that are excited by light. They exhibit enhanced near-field amplitude at the resonance wavelength. This field is highly localized at the nanoparticle and decays rapidly away from the nano-particle/dieletric interface into the dielectric background, though far-field scattering by the particle is also enhanced by the resonance. Light intensity enhancement is a very important aspect of LSPRs and localization means the LSPR has very high spatial resolution (sub wavelength), limited only by the size of nano-particles. Because of the enhanced field amplitude, effects that depend on the amplitude such as magneto-optical effect are also enhanced by LSPRs. In order to excite surface plasmons in a resonant manner, one can use an electron or light beam (visible and infrared are typical). The incoming beam has to match its impulse to that of the plasmon. In case of p-polarized light (polarization occurs parallel to the plane of incidence), this is possible by passing the light through a block of glass to increase the wavenumber (and the impulse), and achieve the resonance at a given wavelength and angle. S-polarized light (polarization occurs perpendicular to the plane of incidence) cannot excite electronic surface plasmons. Electronic and magnetic surface plasmons obey the following dispersion relation:

$$K(\omega) = \frac{\omega}{c} \sqrt{\frac{\varepsilon_1 \varepsilon_2 \mu_1 \mu_2}{\varepsilon_1 \mu_1 + \varepsilon_2 \mu_2}}$$

Where, is the dielectric constant, and μ is the magnetic permeability of the material (1: the glass block, 2: the metal film).

2.3 Discrete plasmon resonances in metal nanoparticles

For a metal nanoparticle, the charge oscillation and field distribution along the surface must be quantized in all three directions. Consequently, the particle supports discrete plasmon modes. In other words, instead of propagating waves described by a wavevector, k, plasmons in nanoparticles form standing waves defined by the geometry of the particle. The lowest-order mode of a spherical particle driven by an external field is illustrated in Figure 5. This mode is dipole-like, with negative charge accumulating on one side of the particle and positive charge accumulating on the opposite side. Field lines converge at the regions where the charges accumulate, corresponding to strong local enhancement of the electric fields. Particles with different shapes will support different modes. For example, a nanorod that is extended in one direction will support longitudinal modes when an external field drives the charge along the long axis of the rod, and will support transverse modes when the charge is driven along the short dimension, as illustrated in Figure 5. The lowest-order longitudinal mode is similar to the lowest-order mode in the sphere, with strong concentration at the rod ends. The transverse mode results in very different field distributions, and occurs at a different frequency than the longitudinal mode.
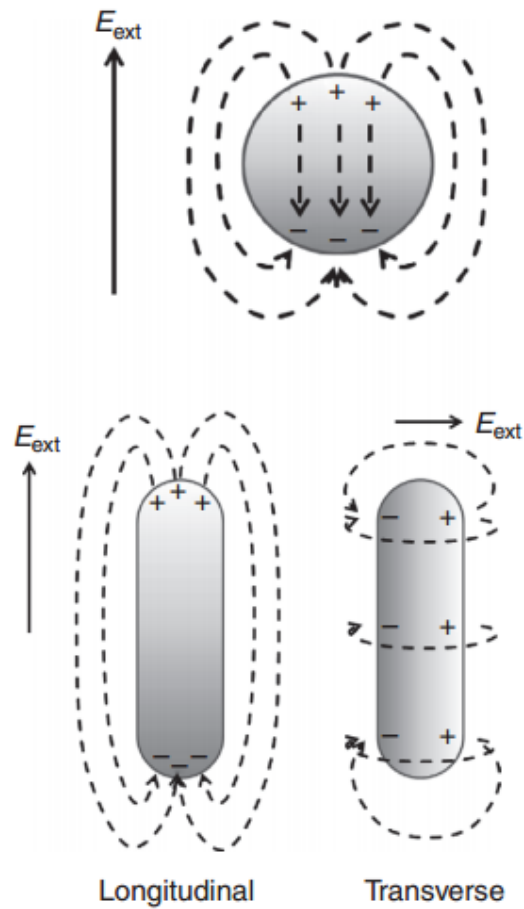
Figure 5 Near-field electric distributions of a nanosphere (top) and nanorods (bottom). The two different modes of a nanorod - based on the direction of external E field

Although the nanoparticle modes occur at discrete frequencies, they are strongly broadened by the significant damping in the metal. They are thus not truly discrete modes, but should rather be thought of as resonances of the structure. At frequencies where metal losses are relatively small, the resonances can be well defined; if metal losses are large, by contrast, the response of the metal nanoparticle becomes broad, and it can be difficult to determine a specific resonance frequency. We will often use the word "mode" to refer to plasmon resonances in metal nanoparticles, but it is important to keep in mind the differences between these rapidly decaying excitations and true eigenmodes. Perhaps the most compelling and intuitive picture of plasmons in metal nanopartices, one which ties together the other two pictures, is that the resonances correspond to displacements of the conduction electron density toward one side of the particle by an applied driving field. This

sets up a restoring force between the negatively charged electrons and the positively charged ion cores that are left behind. If the conduction electron density is incompressible, then charge can accumulate only at the surface, as indicated in Figure 5. Net positive and negative charges appear on opposite surfaces of the nanoparticle, and the strength of the restoring force depends on the distribution of these charges. The restoring force, in turn, defines the oscillation frequency. The plasmon resonance thus depends on the shape of the nanoparticle, which determines how the charge accumulates at different positions on the surface, and on the electron density, which determines the amount of charge that accumulates. The high electron densities in noble metals lead to plasmon resonance at visible and near-infrared frequencies. The surface charges are also responsible for the strong local fields at the surfaces of the particles that arise when the plasmon resonances are excited.
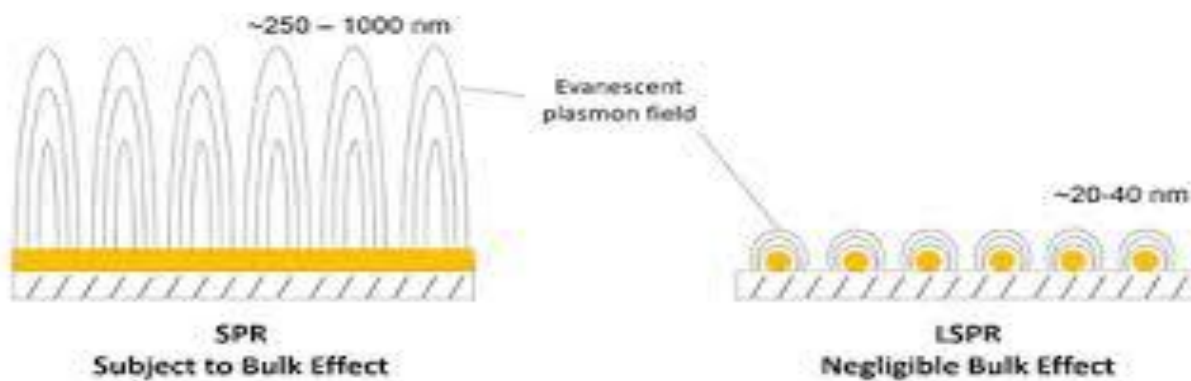
Figure 6 Differences between SPR and LSPR

3. Fano Resonance

3.1 Coupled Plasmons

When the plasmon resonance of one particle in an assembly overlaps spectrally with the resonance of another particle, the two plasmon resonances will couple to one another. This can lead to the emergence of new plasmon modes and can further enhance local fields.

Coupling between plasmon resonances can occur in the near field or in the far field. Far-field coupling occurs when particle separations are comparable to or larger than the optical wavelength. In this case, interaction occurs through fields scattered off the particles. Multiple scattering in an array of nanoparticles can lead to strong diffractive effects and the formation of optical bandgaps, so that the arrays act as a kind of photonic crystal. Here, we focus on near-field coupling of nanoparticles, which occurs when the particle separation is comparable to the extent of the evanescent field at the particle surface. Near-field coupling results from the Coulomb interaction between the surface charges on the different particles. This capacitive coupling is strongest when the regions of the particles with high charge density are next to one another, and the coupling increases when the separation between the particles is reduced. When near-field coupling is strong, large charge dipoles can develop across the gap between the particles, so that the local fields in the gap can be much greater than the sum of the local fields that would be produced by the isolated particles. Material in the gap will also affect the strength of the coupling, producing shifts in plasmon resonance frequencies that can be used for sensitive chemical detection.

3.2 Fano Resonance

There is another way to modify the character of plasmon resonances that does not require electrostatic coupling between modes, but relies on interference instead. When multiple plasmon resonances of a nano-particle system are excited simultaneously, the total response is due to the superposition of the fields produced by each resonance. Interference among these fields can lead to a total response that is very different from the response of the individual resonances acting alone. In particular, if a broad, bright resonance interferes with a narrow, dark resonance, the total response can take on a unique spectral shape known as a Fano resonance. This class of resonances

was first described by Ugo Fano, to explain the appearance of asymmetric peaks in the excitation spectrum of He. In this case, the resonances arose because of quantum-mechanical interference between transition amplitudes for different pathways between an initial and final state, one pathway involving a narrow, discrete level and the other involving a broad continuum. In the case of plasmon resonances, Fano resonances occur due to classical interference between the fields generated by a broad and a narrow resonance. To understand Fano resonances, we first consider how the lineshape of the usual Lorentzian resonance arises, as illustrated in Figure 7. The real component of the field near a normal resonance at ω_r is proportional to $(\omega - \omega_r)/[(\omega - \omega_r)^2 + \gamma^2]$, where γ determines the width of the resonance. This describes a dispersive response that changes sign at ω_r. The imaginary component of the field is proportional to $\gamma/[(\omega - \omega_r)^2 + \gamma^2]$. This describes an absorptive response, with a maximum at ω_r. The overall response function, typically proportional to the the intensity I, follows the same Lorentzian profile as the imaginary component of the field.

A Fano response appears when two modes, a broad mode with field E_B and a narrow mode with field E_N, overlap spectrally. E_B and E_N each, in isolation, follow a Lorenztian response, but with very different values of γ, and potentially with different values of ω_r. When the two modes are excited simultaneously, the total intensity is proportional to $|E_B + E_N|^2$.
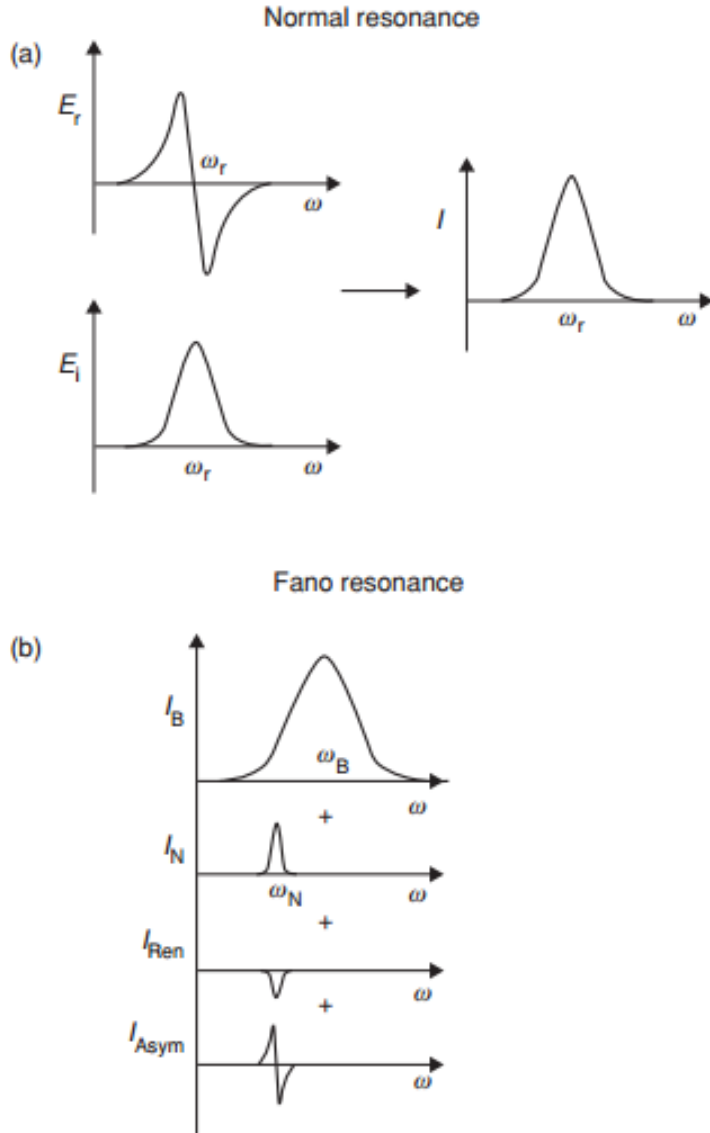
Figure 7 Contributions to (a) Normal resonance and (b) Fano resonance

As illustrated in Figure 7, this total intensity has four contributions. I_B is the broad resonance arising from the broad mode. I_N is the narrow resonance arising from the narrow mode. I_{Ren} results from the interference of the imaginary components of the fields from the two resonances. Near the narrow resonance at ω_N, it is proportional to $[E_{iB}(\omega_N)\gamma_N]/[(\omega - \omega_N)_2 + \gamma_{N2}]$, assuming that E_B is slowly varying around ω_N. I_{Ren} is thus a renormalized version of the narrow resonance: it has the same lineshape, but has a strength that depends on $EB\ i\ (\omega_N)$. Finally, I_{Asym} arises from the interference of the real components and is proportional to $[E_{rB}(\omega_N)(\omega - \omega_N)]/[(\omega - \omega_N)_2 +$

$\gamma N2$] near ωN. It thus has an asymmetric dispersive form that follows ErN, so that it enhances the response on one side of ωN and reduces the response on the other side. The narrow response around ωN due to $IN + I$Ren $+ I$Asym is referred to as the Fano resonance. When IAsym is small compare to IRen, the Fano response has an asymmetic Lorentzian line shape. When I Asym is large compared to IRen, the Fano response takes on a dispersive lineshape. Fano resonances are thus pure interference phenomena, and do not require any coupling between plasmon resonances. However, in real metal nanostructures, plasmon modes generally couple and hybridize at the same time as they interfere. Thus, in general, the effects of interference and hybridization appear simultaneously, Aand can be difficult to clearly separate from one another.

3.3 Mathematical Formulation of Fano Resonance

We have tried to explore the physics and the key concepts behind fano resonance. Firstly, we need to understand what is quantum scattering. From that, we will develop a mathematical formulation for the effective scattering cross-section area. Then we will construct Schrodinger's Wave Equation for a system where quantum scattering takes place and thereby solve the equation. This allows us to construct an energy matrix for the wave. By analysing the energy matrix, we can find out the Fano Resonance.

Now, we will examine a system where a hard sphere (target) is bombarded by a mono-energetic beam of electromagnetic waves. By doing so, we find that there are two kinds of waves that hit the detector. One of them is the incident plane wave while another is the scattered wave.
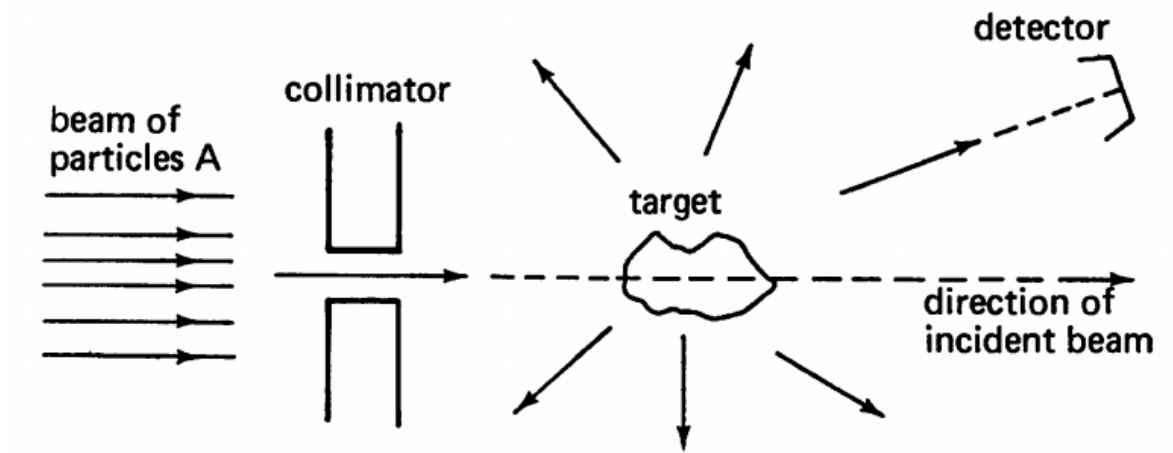
Figure 8 A typical scattering process experimental setup

Now the scattering process can be understood by constructing the Schrodinger's Wave Equation for the whole system and then solving it.

We know the Scrodinger's Wave Equation to be,

$$\left(-\frac{\hbar^2}{2m}\nabla_r^2 + V(r)\right)\Psi(r, t) = i\hbar\frac{\partial}{\partial t}\ \Psi(r, t)$$

As the Schrodinger's Wave equation is a 2nd order differential equation, we can assume that one of the solutions will be in the following form

$$\psi_{k_i}^{(+)}(r) \xrightarrow[r\to\infty]{} A\left(\exp(ik_i \cdot r) + f(\theta, \phi)\frac{\exp(ikr)}{r}\right)$$

As we have seen that there are two waves in our system, so it is obvious that the wave equation will consist of two terms. First term denotes the incident wave while the second is the scattered wave. Now, we will rearrange our 1st term in a way so that we can analyse it by looking at the coordinate arrangement of the scattering process.
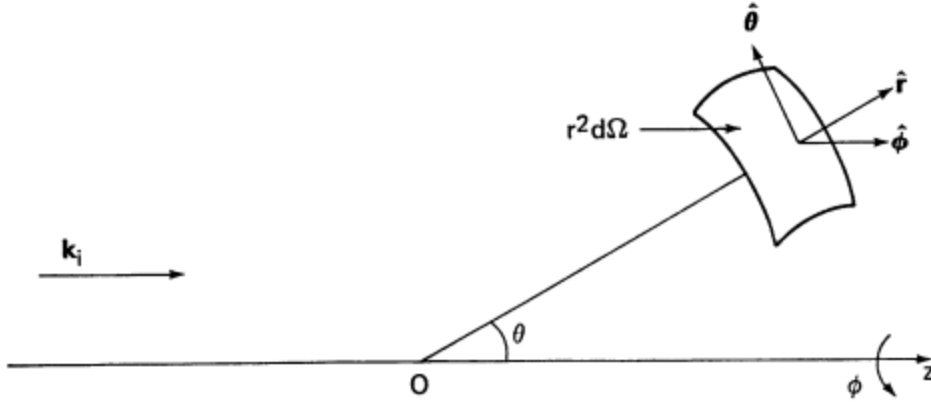
Figure 9 Definitions of angles and coordinate transformation

From the illustration, we can see that our incident wave can be written as

$$\psi_{inc}\left(\mathbf{r}\right) = e^{i\mathbf{kr}} = e^{ikr}\cos\theta$$

Now considering,

$$\rho = kr \qquad \mu = \cos\theta$$

We can rewrite our incident wave equation as

$$e^{i\rho\mu}$$

We can see that Rho is a function of distance (r) and Mu is function of angle (theta).

Thus, Rho and Mu can be written in the form of Legendre polynomial ($P_l^m cos(Q)$)(which itself is a function of angle) and spherical Bessel function ($j_l(x)$)(function of distance). After rearranging, we can have our equation as

$$e^{i\rho\mu} = \sum_{l=0}^{\infty} a_l p_l\left(\mu\right) j_l\left(\rho\right)$$

; Here, a_l is a constant.

Now the only unknown part of the equation is a_l. So, our target will be find out this term.

WE know that Legendre polynomials are orthogonal. Thus, by using this property and the property of Kronecker delta we can do the following calculation.

$$\int_{-1}^{+1} e^{i\rho\mu} P_{l'}(\mu)d\mu = \sum_{l=0}^{\infty} a_l \left[\int_{-1}^{+1} P_l(\mu) P_{l'}(\mu)d\mu \right] j_l(\rho)$$

$$= \sum_{l=0}^{\infty} a_l \left[\frac{2}{2l+1} \delta_{l'l} \right] j_l(\rho)$$

$$= a_{l'} \left[\frac{2}{2l'+1} \right] j_{l'}(\rho)$$

We can find the solution of this equation using integration property. The solution we find is

$$a_l = i^l (2l + 1)$$; Where a_l is the partial wave amplitude

Thus, we can write

$$e^{ikr\cos\theta} = \sum_{l=0}^{\infty} i^l (2l + 1) P_l \cos(\theta) j_l(kr)$$

By using Spherical Bessel function and integration property we can say that our incident wave is

$$\psi_{inc} \xrightarrow[r\to\infty]{} \frac{1}{2ikr} \sum_l (2l+1) \left[P_l(\cos\theta)e^{ikr} - P_l(-\cos\theta)e^{-ikr} \right]$$

From the collision process we can say that our scattered wave is a phase shifted version of the incident wave. Thus, the wave function of the total system can be written as

$$\psi_{Tot}(\vec{r}) \xrightarrow[r\to\infty]{}$$

$$\frac{1}{2ikr} \sum_l c_l(2l+1) \left[P_l(\cos\theta)e^{i(kr+\delta_l)} - P_l(-\cos\theta)e^{-i(kr+\delta_l)} \right]$$

Where δ_l is the phase shift of lth wave (scattering phase shift).

Here, the only unknown term is c_l (depends on boundary conditions).

$$c_l = e^{\pm i\delta_l}$$

We can find cl by using the boundary conditions and normalization.

$\psi_{Tot}^+ (\vec{r}, t) \big] \rightarrow$ **outgoing wave boundary conditions**

$\psi_{Tot}^- (\vec{r}, t) \big] \rightarrow$ **ingoing wave boundary conditions**

Here, ingoing boundary condition refers to photoionization effect and outgoing boundary conditions to scattering effect. Thus, we will be using outgoing boundary conditions.

Therefore, $Cl = e^{i\delta_l}$

By inserting this value of cl into the equation of total wave function and then comparing it with the assumed solution of Schrodinger Equation mentioned at the beginning, we can show that our scattering wave amplitude is

$$f(k,\theta) = \frac{1}{2ik} \sum_{l=0}^{\infty} (2l+1) \left[e^{2i\delta_l(k)} - 1 \right] P_l(\cos\theta)$$

This is known as the Faxen-Holtzmark's formalism.

Here, each lth term gives the contribution of the lth partial wave to the scattering amplitude.

Thus, the total wave function can be written as

$$\psi_{Tot}^- (\vec{r}, t) \Big]_{r \to \infty} e^{+i(kz+\omega t)} +$$

$$\frac{e^{+i(kr+\omega t)}}{r} \left\{ \frac{1}{2ik} \sum_{l=0}^{\infty} (2l+1) \left[e^{2i\delta_l(k)} - 1 \right] P_l(\cos\theta) \right\}$$

Here the 1st term refers to the incident wave and the 2nd term refers to the scattered wave.

Now, using Neumann and Special Hankel functions we can derive our phase shift to be

$$\delta_l (k) = \varepsilon_l (k) + \rho_l (k)$$

Where 1st term is independent of V(r) but the 2nd is dependent on V(r). Here is epsilon(l)(k) is the hard-sphere component and Rho(l)(k) is the scattered component.

For resonance to occur

$$\delta_l^r = \tan^{-1}[\frac{\Gamma\frac{E}{2}}{E_r - E}]$$

Here, gamma is the resonance width and Er is the resonance energy. At resonance, $\rho \to \delta^r$ in the interval of gamma (outside this region, del(l) is mostly epsilon(l)(k)).

Using only the resonant part (and not considering e^iEpsi(l)(k)), we get

$$f_\ell^r(k,\theta) = \frac{2l+1}{k} \frac{\frac{1}{2}\Gamma}{E_r - E - \frac{1}{2}i\Gamma} P_l(\cos\theta)$$

This is the angle modulation in terms of gamma. Now we need to find the effective scattering cross section using

$$\sigma = \int |f|^2 \, d\theta$$

Thus by carrying out the above intergration, we can find that our total effective scattering cross-section for resonance to occur is

$$\sigma_{tot} \simeq \sigma_l = \frac{4\pi(2l+1)}{k^2} \frac{\Gamma^2}{4(E-E_r)^2 + \Gamma^2}$$

This is known as the Breit-Wigner formula.

From that equation we find

$$\sigma_{tot} = \sum_{l=0}^{\infty} \sigma_{l_k} \quad \textbf{Sum of contributions from all partial waves}$$

$$\sigma_l = \frac{4\pi}{k^2}(2l+1)\left[\sin^2 \xi_l(k) + \frac{\frac{1}{4}\Gamma^2}{(E_r-E)^2 + \frac{1}{4}\Gamma^2} + 2\sin\xi_l(k)\frac{1}{2}\Gamma \, \mathrm{Re}\left(\frac{e^{i\xi_l(k)}}{E_r - E - \frac{1}{2}i\Gamma} \right) \right]$$

'pure' background part

'pure' resonance part

'interference'

After calculating the real part of the interference term, we can write the following equation

$$\sigma_l = \frac{4\pi}{k^2}(2l+1)\left[\sin^2 \xi_l(k) + \frac{\frac{1}{4}\Gamma^2}{(E_r-E)^2 + \frac{1}{4}\Gamma^2} + 2\sin\xi_l(k)\left(\frac{1}{2}\Gamma\right)\frac{(E_r-E)\cos\xi - \frac{1}{2}\Gamma\sin\xi}{(E_r-E)^2 + \left(\frac{1}{2}\Gamma\right)^2} \right]$$

Now, considering the following

$$a = E_r - E \quad ; \quad b = \frac{1}{2}\Gamma$$

We can rearrange the previous equation as

$$\sigma_l = \frac{4\pi}{k^2}(2l+1)\left[\sin^2 \xi_l(k) + \frac{b^2}{a^2+b^2} + 2\sin \xi_l(k)b \frac{a\cos\xi - b\sin\xi}{a^2+b^2}\right]$$

Now, considering Fano parameters

$$\varepsilon = -\cot \delta_\ell^r = -\frac{a}{b}$$

$$q = -\cot \xi_\ell$$

$$\tan \delta_\ell^r = -\frac{1}{\varepsilon} = \frac{b}{a}$$

We can further rearrange the equation to be

$$\sigma_l = \frac{4\pi}{k^2}(2l+1)\sin^2 \xi \frac{(q+\varepsilon)^2}{1+\varepsilon^2}$$

This is the scattering cross section for Fano Resonance.

Full form of scattering cross section can be simplified using Fano parameters. These parameters will be crucial in defining the Fano line shape.

$$\varepsilon = -\cot \delta_\ell^r = -\frac{a}{b}$$

$$q = -\cot \xi_\ell$$

$$\tan \delta_\ell^r = -\frac{1}{\varepsilon} = \frac{b}{a}$$

Classical calculation will give us the Lorentz lineshape. But in quantum mechanical approach we get the accurate picture which consist of a peak and a dip within same resonance width. This is dip is due to the presence of a tangent function.
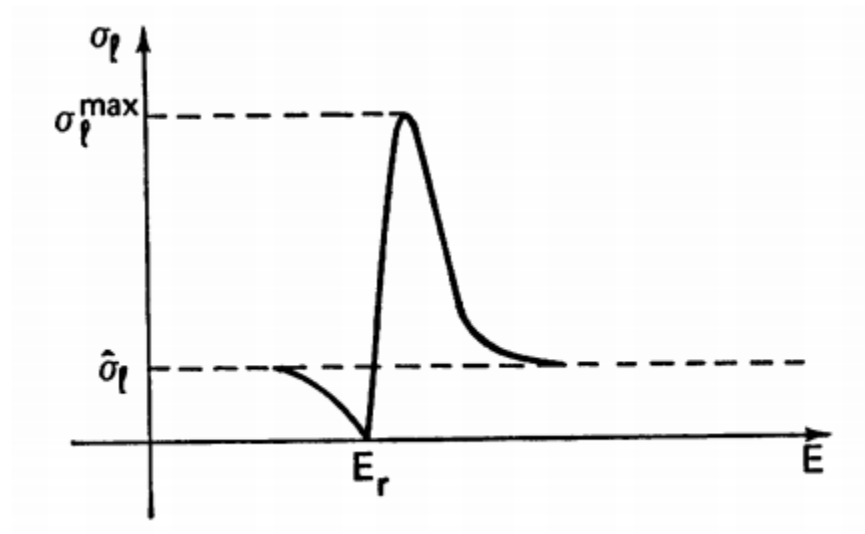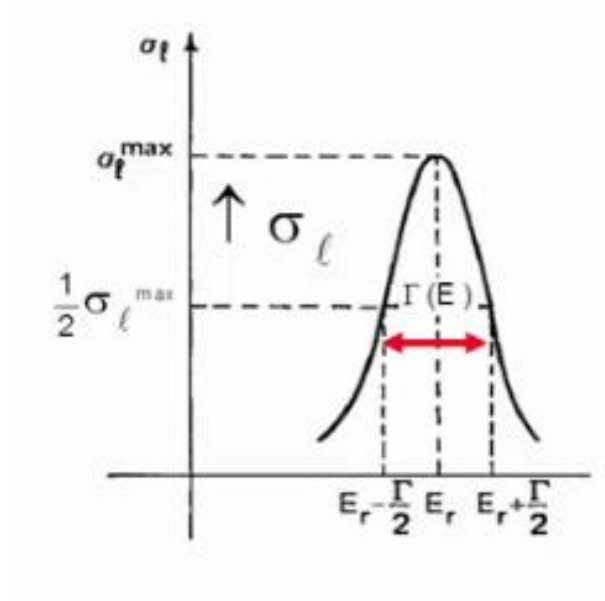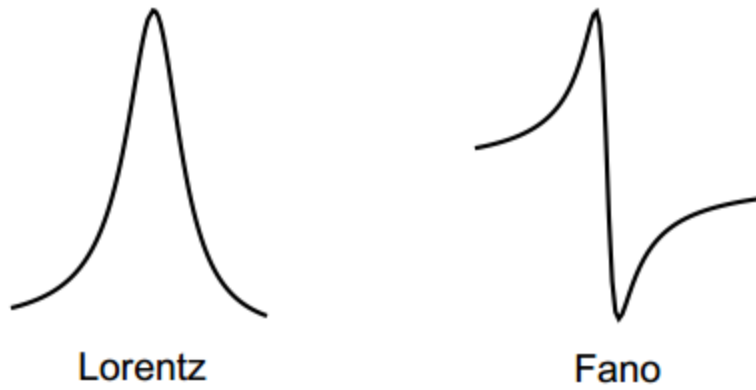
Figure 10 The Lorentz and Fano lineshapes

Fano's quantum mechanical model

$$\langle\psi_d|H|\psi_d\rangle = E_d \,,$$
$$\langle\psi_{E'}|H|\psi_d\rangle = V_{E'} \,,$$
$$\langle\psi_E|H|\psi_{E'}\rangle = E'\delta(E' - E)$$

Energy matrix; where Ed is discrete energy of discrete state Shi(d)

And, E' is the continuum energy of continuum state Shi(e)

Eigenvector of energy matrix

$$\chi_E = a\psi_d + \int dE' b_{E'}\psi_{E'}$$

Formal solution of system of equations

$$b_{E'} = \left[\frac{1}{E - E'} + z(E)\delta(E - E') \right] V_{E'a}$$

Reduced energy (Fano parameter)

$$\epsilon = -\cot\Delta\phi = \frac{E - E_d - F}{1/2\Gamma}$$

Here, Gamma is the spectral width of autoionization state Shi(d)

Zero of the resonance

$$q = \frac{\langle \Psi_d | T | i \rangle}{\pi V_E^* \langle \psi_E | T | i \rangle}$$

q is the transition ratio of discrete and continuum states and also shows the degree of asymmetry of the resonance.

Transition probability; interferes with opposite phase on two sides of the resonance

$$\frac{|\langle \chi_E | T | i \rangle|^2}{|\langle \psi_E | T | i \rangle|^2} = \frac{(\epsilon + q)^2}{\epsilon^2 + 1}$$
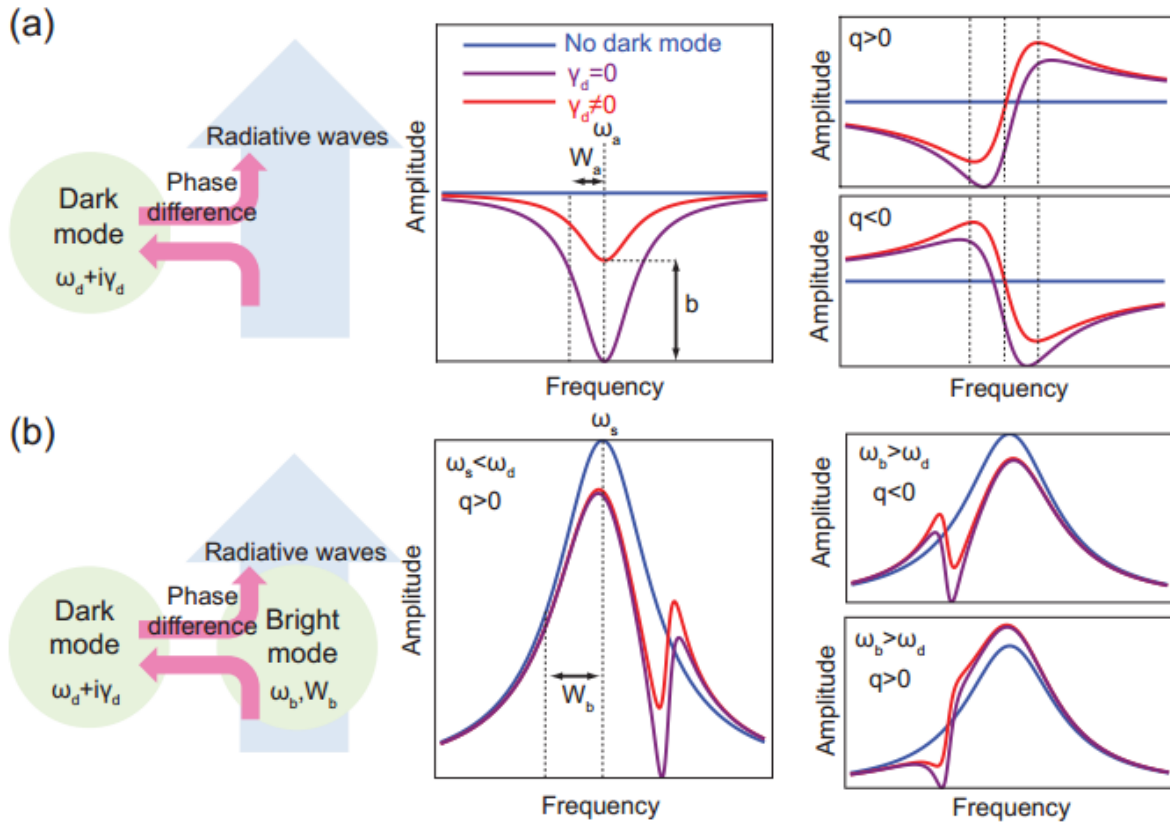
Figure 11 The dark and bright modes

Analytical function (dark mode)

$$\sigma_a(\omega) = \frac{\left(\frac{\omega^2 - \omega_a^2}{\Gamma} + q\right)^2 + b}{\left(\frac{\omega^2 - \omega_a^2}{\Gamma}\right)^2 + 1}$$

Modulation damping parameter

$$b = \frac{\Gamma_i^2/\Gamma_c^2}{(1 + \Gamma_i/\Gamma_c)^2}$$

33

Pseudo-lorentzian line shape (bright mode)

$$\sigma_b(\omega) = \frac{a^2}{\left(\frac{\omega^2 - \omega_b^2}{\Gamma_b}\right)^2 + 1}$$

Total strength of Fano resonance

$$\sigma_{tot}(\omega) = \sigma_b(\omega)\sigma_a(\omega)$$

4. Bimetallic Nanorods

4.1 Structures and optical properties of 4–5 nm bimetallic Ag-Au nanopartilces

Nanoparticles comprising two different metallic elements offer additional degrees of freedom for altering their physical properties by varying the atomic composition and atomic arrangement. This could potentially enable a wide range of opportunities for discovering materials with novel physical properties. However, our present under- standing of fundamental issues, such as the driving force for generating specific structures of bimetallic nanoparticles, as well as structure–property correlations, has been hindered by the lack of size control and knowledge of the precise chemical composition and atomic arrangement within a given bimetallic nanoparticle. The situation is most acute for nanoparticles less than a few nanometres in diameter. Currently it is still a significant challenge to synthesis and to characterize, with atomic precision, bimetallic nanoparticles with sizes smaller than about 5 nm.

Bimetallic Ag-Au nanoparticles have been chosen as a model system. This is probably one of the most studied bimetallic systems in the literature, partly because both Ag and Au nanoparticles display distinctive optical plasmon absorbance's in the visible range, with size and shape dependent properties. In the bulk, Ag and Au form alloys for all compositions with very little surface segregation due to their very similar lattice constants, 4.09 A and 4.08 A˚, respectively. However, nanoparticles with either alloyed, or core–shell segregated structure can be synthesised through various methods. As a consequence, the optical properties of these bimetallic particles can be tuned not only by varying their size and external morphology, but also by changing their composition and internal structure (chemical ordering).

In fact, optical absorption spectroscopy has been the most widely used technique for inferring the internal structure of the Ag–Au nanoparticles.

Often, a single plasmon band has been used to indicate that the Ag–Au particles have an alloyed form, while the appearance of two distinct plasmon peaks has been used as a fingerprint for segregated bimetallic nanoparticles. In practical terms, this approach is simple, but is only appropriate for Ag–Au nanoparticles with particle sizes between 10–100 nm. In the case of smaller core–shell particles, the

situation is more complicated, as the plasmon resonance absorbance energy depends not only on composition but also on nanostructure. While the outermost shell of the materials might dominate the interaction with the incident light for shell thicknesses larger than the frequency dependent absorbance length, the electron plasmon oscillations will also be damped by any interface between the metals, changing the shape of the absorbance curve. The optical contributions from the core material may be effectively screened for large shell thicknesses. In any case, optical measurements provide number average information that may not reflect the heterogeneous nature of bimetallic nanoparticles. Therefore, it is extremely important to develop methods having a high spatially-resolved imaging capability for the internal structure to correlate nanostructure with optical properties. This will provide us with the knowledge of the actual structure of the as-synthesized nanoparticles and how changes in nanostructure over time affect the optical absorbance. High resolution imaging of individual nanoparticles will also provide the detailed inputs needed for accurate modelling to understand the underlying physical mechanisms that favour either mixing or segregation in bimetallic nanoparticles.
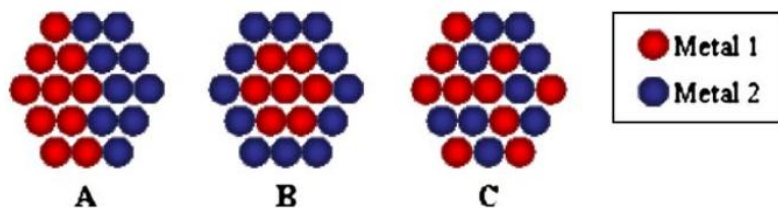
Figure 12 Structures of bimetallic nanoparticles. (A) Separated, (B) Core-shell, and (C) Random

4.2 Recent Advances in the Synthesis of Plasmonic Bimetallic Nanoparticles

One of the most promising areas of research for these bimetallic structures is for their unique plasmonic properties. A number of synthetic approaches have been developed for the synthesis of plasmonic bimetallic nanoparticles with controlled morphology. These include wet chemical synthesis, sonochemical synthesis, photochemical synthesis, microwave synthesis, sputter deposition, electroless plating, and electro-chemical synthesis. Depending on the synthetic approach used in the preparation of bimetallic nanoparticles, the distribution of each metal within a particle and their organization will vary to adopt either core–shell,

Random or separated structures, as shown in Fig.12 such structural differences significantly affect the plasmonic properties of bimetallic particles. In the case of core–shell nanoparticles, Mie

scattering theory predicts that the plasmon resonance can be shifted between the ultraviolet (UV) to the midinfrared (IR) region by varying the shell thickness ratio to the overall size. Gold (Au), silver (Ag), and copper (Cu) nanoparticles display well-known surface plasmon resonance (SPR) bands as a result of the coherent oscillations of the conduction band electrons induced by the interacting electromagnetic field. However, the coupling of one of the above metals with another metal to form bimetallic nanoparticles influences the chemical and physical properties of the overall particle. Some of these effects have been noted for catalytic and sensor applications. For continued advancements in plasmonics, novel nano-structures need to be developed that exhibit unique properties. Because of this, much of the recent effort in this field has been in the development of new techniques for synthesis of these bimetallic nanoparticles. These techniques have been shown to both improve on previous methods and to generate unique morphologies and sizes which could prove to be valuable in various applications. This review focuses mainly on the synthesis and fabrication of these bimetallic nanostructures that exhibit Plasmonic effects. In later sections, characterization techniques used to study these particles are briefly covered, as well as future perspectives in the field. The underlying theory behind SPR is defined by the Mie solutions to Maxwell's equations. To translate to a bimetallic system, one must first examine the work by Stern and Ferrell, which showed that an interface plasmon mode can exist at the boundary between two metals.

For the case of a bimetallic particle, the two different metals have different electron densities and, therefore, two different plasma frequencies. Because of this, it was shown that, at the bimetallic interface, the resonant frequency w of the plasma wave is given by:

$$\omega = \left[\tfrac{1}{2}\left(\omega_p^2 + \omega_p'^2\right)\right]^{\tfrac{1}{2}}$$

Where wp is the classical plasma frequency and w0p represents a different plasma frequency based off the dielectric constant at the interface.

Metals, such as silver and gold, are not purely free-electron materials. Therefore, interband contributions into their dielectric functions must be taken into account at certain wavelengths. To account for bimetallic structures, the dielectric function used is a weighted linear combination of

dielectric constants of the constituent metals. Probably the most interesting property of bimetallic nanoparticles is the ability to tune their plasmon resonances
across a wide range.

4.3 Bimetallic nanoparticles: Preparation, properties, and biomedical application

Optical properties of Au–Ag

Plasmonic coupling between NPs is one of the most interesting optical properties; the characteristic improvement of local optical field at particle–particle interface is extremely useful for numerous sensing applications. Monometallic Ag and Au NPs have relatively monotonous optical properties due to surface plasmon resonance (SPR); the SPR properties of Ag–Au alloy NPs are incessantly tunable because of the possibility of composition changes. SPR excitation
within the gold and silver nanostructures greatly enhances the local electric field. The absorption and dispersion of light in NPs rely on the characteristic of the metals, including their chemical composition, morphology, and size. NPs of noble metals, for instance gold and silver, with a size smaller than the wavelength of visible light powerfully scatter and absorb light because of SPR. Au–Ag BMNPs show diverse optical responses for alloy and core–shell configurations, even when they have the same Au and Ag contents.

There are significant differences among the dielectric functions of different metals. Figure 1.3 compares empirical for Au, Ag, and Cu [6]. The R for the three metals appear to be similar, with the Drude contribution dominating at low frequencies and interband contributions prominent at higher frequencies. However, the expanded view shows there are important differences when R is near zero, the region important for plasmonics, due to the different frequencies at which interband transitions begin to occur. The differences in R mean that plasmon resonances for a particular nanoparticle shape will occur at different frequencies for the different metals. Even more importantly, the interband transitions produce large changes in I, corresponding to large differences in plasmon damping. Ag has a wide window of low I, and supports plasmon resonances with the lowest losses of all materials throughout most of the visible and near-infrared spectral regions. Cu has a much smaller window of lower losses, and is therefore not commonly used for plasmonic applications. Au is intermediate between the two other metals. However, Au is more

chemically stable than Ag, and is therefore often used as the material of choice for plasmonic studies, despite having larger losses than Ag.

4.4 Analyzed Structure

The proposed structure of the thesis is the arrangement of two metal nanorods, Aluminum (Al) and Silver (Ag) arranged by end-to-end with a small gap in between. Although Fano Resonance is known to have a lesser extent in heterogeneous nanostructure constituted by nanoparticles of different metals both theoretically and experimentally concentrating on Au-Ag heterodimers but this paper presents a theoretical proof of Fano Resonance in a new kind of heterogeneous metallic nanostructure of Al-Ag nanorods. It is found out that Al nanorods exhibit high tunable plasmonic resonance from deep ultraviolet to visible wavelength region. The experimental setup is shown below:
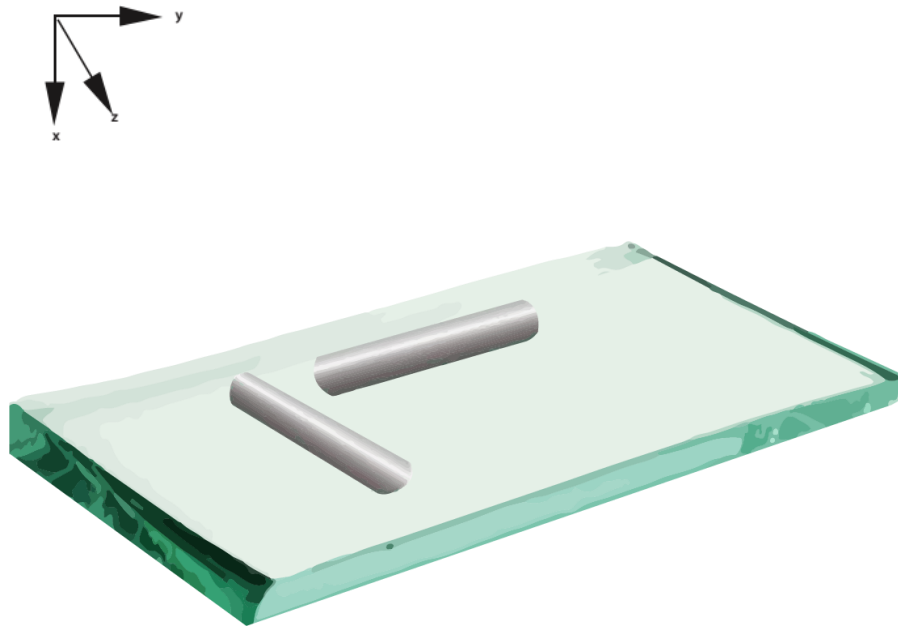
Figure 13 Schematic of structure used in simulations

The short nanorod is the Al nanorod, which supports a broad bright mode, and the longer nanorod is the Ag nanorod that supports a narrow dark mode. The nanorods are placed on top of a substrate of SiO2 (glass). The whole of it is then immersed in water and the entire setup is illuminated with light. Initially the Al rod is 142nm long and the Ag rod is 200nm, both their diameters are 2R=40nm and the gap between them is d=10nm. The Fano dip can be tuned by changing various aspects of the setup. First the power absorption curve for the change in d is noted, keeping the length and diameter constant, followed by the change in length of one rod at a time again keeping the d and diameter constant. Then the change in the Fano dip with change in refractive index is noted and calculated and finally with different protein molecules. The later part of the paper will demonstrate the complete experiment in detail with supporting proofs and curves.

5.Biomolecules

5.1 Protein as a Biomolecule

Any type of molecule, which are present in living organisms, are said to be biomolecule or biological molecule. Biological molecule can be large molecules or can be small molecules as well. Large molecules are carbohydrates, proteins, starch lipids, nucleic acids and so on. Small molecules are primary metabolites, secondary metabolites and natural products. Main elements of biomolecules are carbon and hydrogen with nitrogen, oxygen, sulphur and phosphorus. Chemically, protein is composed of amino acids, which are organic compounds made of carbon, hydrogen, nitrogen, oxygen or sulfur. Amino acids are the building blocks of proteins, and proteins are the building blocks of muscle mass, according to the National Institutes of Health (NIH)

The biomolecules or proteins are used for the thesis is given below:

Protein	Shape	Dimension (nm)			Mass (kDa)	Refractive Index
		Major axis	Minor axis-1	Minor axis-2		
Lys	Ellipsoid	4.5	1.8	1.8	14.3	1.495
HSA	Ellipsoid	7.5	6.5	4	66.4	1.445
Abn	Ellipsoid	7.4	7.2	7.2	150	1.45
CAT	Ellipsoid	9.7	9.2	6.7	230	1.465
Fb	Elongated ellipsoid	46	6	3	390	1.39

5.11 Lysozyme (Lys)

In the early twentieth century lysozyme was discovered by Alexander Fleming. Lysozyme is a special type of enzyme which can be found in salvia, sweat, breast milk, tears and other type of body fluids. It is also found in egg white. It mainly works as antibacterial enzyme. Lysozyme is capable of destroying the growth of bacteria. Carbohydrate and Peptidoglycan layer are the elements which are present in the cell walls of bacteria and lysozyme breaks down the elements, in this way it can stop the growth of bacteria. It catalyzes the hydrolysis of 1,4-β linkages between N-acetylmuramic acid and N-acetyl-D-glucosamine. The enzyme functions by attacking peptidoglycans (found in the cell walls of bacteria, especially Gram-positive bacteria) and hydrolyzing the glycosidic bond that connects *N*-acetylmuramic acid with the fourth carbon atom of N-acetylglucosamine. It does this by binding to the peptidoglycan molecule in the binding site within the prominent cleft between its two domains. This causes the substrate molecule to adopt a strained conformation similar to that of the transition state. According to Phillips-Mechanism, the lysozyme binds to a hexasaccharide. The lysozyme then distorts the fourth sugar in hexasaccharide (the D ring) into a half-chair conformation. In this stressed state, the glycosidic bond is easily broken.
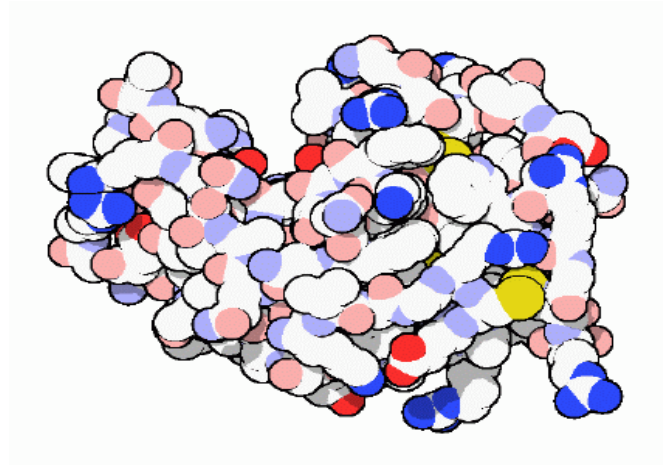
Figure 14 Structure of Lysozyme

Lysozymes plays different role in different type of cancers. Cancer cells can create lysozyme in such a huge amount that high concentration of lysozyme can be found on blood stream. The increased amount of lysozyme in blood causes kidney disorder or kidney failure. It also decreases the amount of potassium and electrolyte levels in blood. If doctors remove the malignant tumor then this situation can be improved.

5.12 Human Serum Albumin (HSA)

Serum albumin present in human blood is said to be the human serum albumin. This serum is soluble, monomeric and produced in liver. It is a globular protein of 585 amino acids. The amount of HSA in blood is the almost 60% of the total protein present in blood serum. Albumin is synthesized in the liver as preproalbumin which has an N-terminal peptide that is removed before the nascent protein is released from the rough endoplasmic reticulum. The product, proalbumin, is in turn cleaved in the Golgi vesicles to produce the secreted albumin. Albumin is a soluble, monomeric protein which comprises about one-half of the blood serum protein.
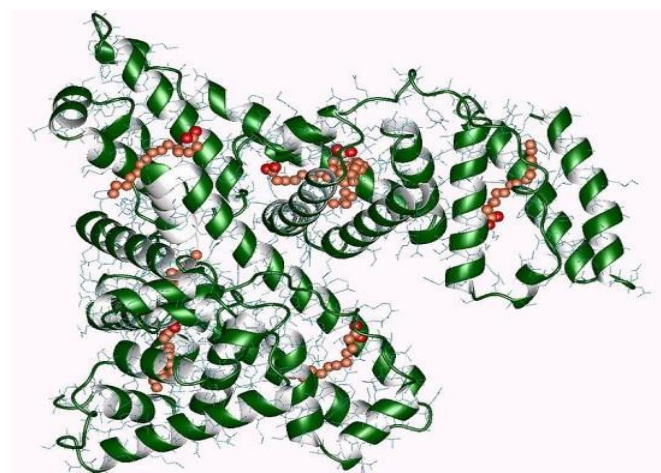
Figure 15 Structure of HSA

Albumin functions primarily as a carrier protein for steroids, fatty acids, and thyroid hormones and plays a role in stabilizing extracellular fluid volume. Mutations in this gene on

chromosome 4 result in various anomalous proteins. Albumin is a globular unglycosylated serum protein of molecular weight 65,000. The human albumin gene is 16,961 nucleotides long from the putative 'cap' site to the first poly (A) addition site. It is split into 15 exons which are symmetrically placed within the 3 domains that are thought to have arisen by triplication of a single primordial domain. HSA is widely used to stabilize blood volume generally from donors but the fear of contamination such as HIV & Hepatitis has enticed great interest in the recombinant form which is identical to the natural blood. Suitable for use in biochemical, excipient (an inert substance used as a diluent or vehicle for a drug), culture media and chromatographic applications.

5.13 Catalase

Catalase is a common enzyme found in nearly all living organisms exposed to oxygen (such as bacteria, plants, and animals). It catalyzes the decomposition of hydrogen peroxide to water and oxygen. It is a very important enzyme in protecting the cell from oxidative damage by reactive oxygen species (ROS). Likewise, catalase has one of the highest turnover numbers of all enzymes; one catalase molecule can convert millions of hydrogen peroxide molecules to water and oxygen each second.

Catalase is a tetramer of four polypeptide chains, each over 500 amino acids long. It contains four porphyrin heme (iron) groups that allow the enzyme to react with the hydrogen peroxide. The optimum pH for human catalase is approximately 7, and has a fairly broad maximum (the rate of reaction does not change appreciably at pHs between 6.8 and 7.5). The pH optimum for other catalases varies between 4 and 11 depending on the species. The optimum temperature also varies by species.
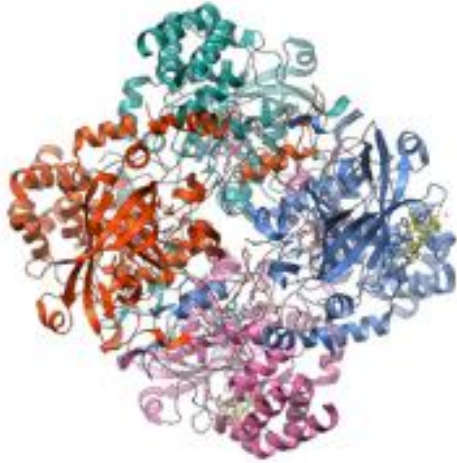
Figure 16 Structure of Catalase

The reaction of catalase in the decomposition of hydrogen peroxide in living tissue:

$$2\ H_2O_2 \rightarrow 2\ H_2O + O_2$$
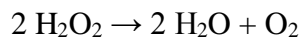
The presence of catalase in a microbial or tissue sample can be tested by adding a volume of hydrogen peroxide and observing the reaction. The formation of bubbles, oxygen, indicates a positive result. This easy assay, which can be seen with the naked eye, without the aid of instruments, is possible because catalase has a very high specific activity, which produces a detectable response. Alternative splicing may result in different protein variants.

Hydrogen peroxide is a harmful byproduct of many normal metabolic processes; to prevent damage to cells and tissues, it must be quickly converted into other, less dangerous substances. To this end, catalase is frequently used by cells to rapidly catalyze the decomposition of hydrogen peroxide into less-reactive gaseous oxygen and water molecules.

Human catalase works at an optimum temperature of 37 °C.

5.14 Fibrinogen

Fibrinogen (*factor I*) is a glycoprotein in vertebrates that helps in the formation of blood clots. It consists of a linear array of three nodules held together by a very thin thread which is estimated to have a diameter between 8 and 15 Angstrom (Å). The two end nodules are alike but the center one is slightly smaller. Measurements of shadow lengths indicate that nodule diameters are in the range 50 to 70 Å. The length of the dried molecule is 475 ± 25 Å. The fibrinogen molecule is a soluble, large, and complex 340 kDa plasma glycoprotein, that is converted by thrombin into fibrin during blood clot formation. It has a rod-like shape with dimensions of $9 \times 47.5 \times 6$ nm and it shows a negative net charge at physiological pH (IP at pH 5.2). Fibrinogen is synthesized in the liver by the hepatocytes. The concentration of fibrinogen in the blood plasma is 200–400 mg/dL (normally measured using the Clauss method). During normal blood coagulation, a coagulation cascade activates the zymogen prothrombin by converting it into the serine protease thrombin. Thrombin then converts the soluble fibrinogen into insoluble fibrin strands. These strands are then cross-linked by factor XIII to form a blood clot. FXIIIa stabilizes fibrin further by incorporation of the fibrinolysis inhibitors alpha-2-antiplasmin and TAFI (thrombin activatable fibrinolysis inhibitor, procarboxypeptidase B), and binding to several adhesive proteins of various cells. Both the activation of factor XIII by thrombin and plasminogen activator (t-PA) are catalyzed by fibrin. Fibrin specifically binds the activated coagulation factors factor Xa and thrombin and entraps them in the network of fibers, thus functioning as a temporary inhibitor of these enzymes, which stay active and can be released during fibrinolysis. Research from 2011 has shown that fibrin plays a key role in the inflammatory response and development of rheumatoid arthritis.
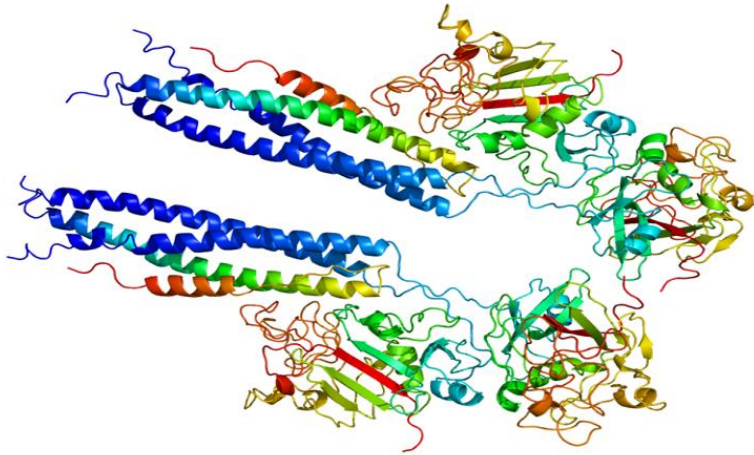
Figure 17 Structure of Fibrinogen

The usefulness of fibrinogen as a marker of inflammation, trauma and various types of infections have been reported in a number of scientific papers

• ☐ **General inflammatory response due to an infection:** Fibrinogen normally increases within 24 to 48 hours from a normal level of 2-4 g/L and may exceed 10 g/l on day 4 - 7 post infection. It is not uncommon in horses to have increased plasma fibrinogen levels as the sole indicator of inflammation.

• ☐ **Surgical trauma:** Levels of serum amyloid A, fibrinogen and iron reflect the intensity of the surgical trauma, whereas WBC do not do this. Fibrinogen is therefore a good diagnostic marker to monitor the healing process after a surgical procedure.

• ☐ **Bacterial infection:** The fibrinogen level can be used to predict the time course of an bacterial infection as has been shown with Escherichia coli endotoxin. It has also been shown to be an effective screening tool to diagnose Rhodococcus Equi infections in foals. Fibrinogen concentrations has also been shown to enable a more precise diagnosis of the severity of an inflammation than that based simply on clinical conditions in respiratory diseases, particularly bacterial pneumonia.

• ☐ **Viral infection:** Horses with equine influenza and herpes virus 2 has been proven to show elevated fibrinogen levels 3 days post infection.

• ☐ **Parasite infection:** Parasitized (Strongelus Vulgaris) ponies showed in a study to have significantly elevated fibrinogen levels compared to a control group 9, 14, 21 and 45 days

after   infection.   *Heidmann*

•☐**Aseptic arthritis:** Experimentally induced aseptically inflammation showed a significant increase in fibrinogen with a maximum level 3 - 6 days post-injections.

5.2 Summary

Any type of molecule, which are present in living organisms, are said to be biomolecule or biological molecule. Main elements of biomolecules are carbon and hydrogen with nitrogen, oxygen, sulphur and phosphorus. These biomolecules has a universal name which is biological material. In the sector of biology and biochemistry, biomolecules and their reactions are considered for research and analysis. These molecules are consists of hydrogen, carbon, nitrogen, oxygen and sulfur.

Lysozyme is a special type of enzyme which can be found in salvia, sweat, breast milk, tears and other type of body fluids. It is also found in egg white. It mainly works as antibacterial enzyme. Lysozyme is capable of destroying the growth of bacteria. Carbohydrate and Peptidoglycan layer are the elements which are present in the cell walls of bacteria and lysozyme breaks down the elements, in this way it can stop the growth of bacteria. It catalyzes the hydrolysis of 1,4-β linkages between N-acetylmuramic acid and N-acetyl-D-glucosamine. Serum albumin present in human blood is said to be the human serum albumin. This serum is soluble, monomeric and produced in liver. It is a globular protein of 585 amino acids. The amount of HSA in blood is the almost 60% of the total protein present in blood serum. Albumin is synthesized in the liver as preproalbumin which has an N-terminal peptide that is removed before the nascent protein is released from the rough endoplasmic reticulum. Human γ-chain was split by low concentrations of trypsin and the digests were analyzed by SDSPAS gel electrophoresis. A number of discrete bands appeared in time with apparent mol. wt of
(in thousands) 43, 31, 25, 18, and 12, while the molecular weight of the γ-chain was 56,000 by this method. These values are in agreement with preferential splitting of the γ-chain between, but not inside, the four domains (homology regions), assuming that the carbohydrate side chain on *Cγ*2 contributes an apparent mol. wt increase of about 6000, and independent of the size of the peptide chain to which it is attached.

Fibrinogen (*factor I*) is a glycoprotein in vertebrates that helps in the formation of blood clots. It consists of a linear array of three nodules held together by a very thin thread which is estimated to have a diameter between 8 and 15 Angstrom (Å). The two end nodules are alike but the center one is slightly smaller. Measurements of shadow lengths indicate that nodule diameters are in the range 50 to 70 Å. The length of the dried molecule is 475 ± 25 Å.

6. Lumerical

6.1 About lumerical

The name Lumerical is a compound word consisting of two words: the fore word '*Luminous*' meaning full of light, illuminated and '*Numerical*' meaning of or relating to a number or a series of numbers; as it is advertised in the company's own website. Their tagline being, "Achieve more with light".

Figure 18 Lumerical logo and logos of different softwares

As their name suggests the company develops software that simulates photonic interaction, tools that help the designers to understand light and predict its interaction with structures, circuits and systems. Lumerical's design tools allow scientists to create, test, and optimize their product designs without crafting physical prototypes. These predictive capabilities enable the scientific and engineering community to validate designs prior to manufacturing, create new product concepts, and explore long-term innovative photonics research. The company provides 4 different software for component design, FDTD Solutions, MODE Solutions, DEVICE Charge Transport, DEVICE Heat Transport. Among these we shall only use FDTD Solutions for our purposes.

6.2 FDTD solutions

This software from **Lumerical** is a high performance 3D Finite Difference Time Domain (FDTD) method Maxwell solver for the design, analysis and optimization of Nano photonic devices, processes and materials. It has various applications and key applications include:

CMOS Image Sensors.

- Solar Cells.
- OLEDs.
- Integrated Optics.
- Surface Metrology.
- Surface Plasmons.
- Metamaterials.
- Photonic Crystals.
- Liquid Crystals.
- Graphene.

Structure modelling

At first the software is installed and opened. Four windows appear on the screen, each with a significance of its own. The top left window shows the 'xy' plane, the bottom left window shows the 'xz' plane, the bottom right window shows the 'yz' plane and the top right window displays the 3D ('xyz') illustration of the particle. On the left of it there is a panel for the objects tree that shows the things we have in the system we are trying to build. Above the four windows rest a panel that shows a list of materials, structures, attributes, components, sources, analysis and monitors we can get for the modeling of our system. Last but not least the top right shows a panel to check all the resources and memory requirements to run the simulation and a button to actually run it.

First, we go to the "Settings" and set the length units to nanometers as we are working with nanoparticles and structures here. Now, we have to make the 2 nanorods in their baseline state. The baseline state in our case being the length of the Ag nanorod is 200 nm and the length of the

Al nanorod is 142 nm while the gap between them in 10 nm and they both have a radius of 20 nm. We go to Components > Cylindrical > Rounded Cylinder. This structure comes as a structure group which means it is a cylinder with two spheres at each end to make a rod or a rounded cylinder. We have to place two of these rods to simulate the Al and the Ag nanorod. Next, we have to select the nanorod on top and make it into the desired Ag nanorod. By right clicking on the structure group we access the option to edit that object. In the editing panel of the object we get to look at the script that runs the simulation for that object. We can change its index, material, radius, radius ends, and z span where index means refractive index; radius is the radius for the cylinder and radius ends is the radius for the spheres at the end and lastly z span means the length of the cylinder. Then, we hop on to the properties tab to change all our variables. Here we want our rods to be long and variable on the y axis. Therefore, the origin points are set (-16.25, 54.8, 0) for (x, y, z) axis. The refractive index is set to 1.4 for Ag and so is the material selected from library as Ag (Silver) – Johnson and Christy. Both radius and radius ends are 20 nm. And the z span (length) is changed to 200 nm for the baseline test. Following the same procedure for the bottom rod we make the Al nanorod. This one uses the material Al (Aluminium) – CRC and has a length of 142 nm. Both nanorods are named as Ag_cyl and Al_cyl for identification later.
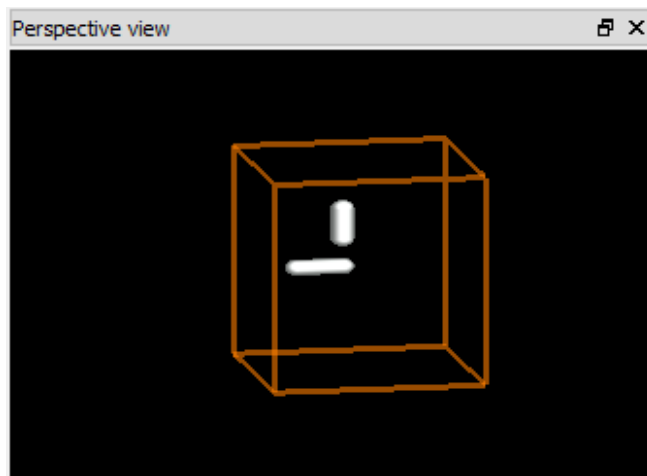

Figure 19 Structure modelling

6.3 Substrate formation

We have already created our nanorods but we still have to create the substrate that the rods have to be placed on. The substrate can be created from various types of materials. For our simulation we shall be using Glass (SiO2). SiO2 is basic sand glass. It is indeed very cheap. Now, in order to

apply the substrate to our setup, we take the following directions "Structure > Rectangle". Then we edit this object according to our necessities; we change the "Geometry" of the rectangle. There are six options: x (nm), y (nm), z (nm), x span (nm), y span (nm) and z span (nm). The values of y and z are set to 0. The values of y and z spans are 600 nm each. The value of x is set to 152.45 nm and the value of x span is set to 295.5 nm. The x, y, z values represent the origin point of the substrate. And the spans represent its width along each axis. The values of the geometry of the substrate are set with accuracy so that the substrate only touches our nanorods on the positive 'y' side on the 'xy' view. The refractive index of Silicon Dioxide is 1.46 and there are a few advantages of using Silicon Dioxide over other substrates.

Advantages of Silicon Dioxide:

- Outstanding thermal stability.
- Low expense coefficient.
- Compressive stress preload.
- High strength (1 GPa) and stiffness.
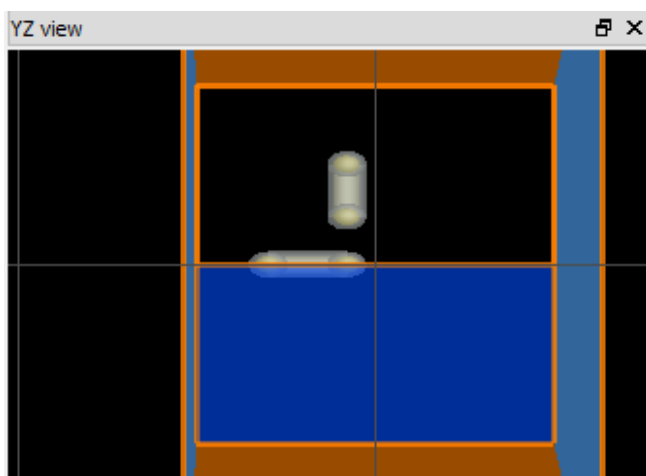- Excellent thickness control.
- Easily reworked die attach

Figure 20 Applying FDTD and placing substrate

This completes the formation of our basic structure of two closely placed nanorods on a glass substrate surface.

6.4 FDTD – Finite Difference Time Domain

FDTD allows us to change the surroundings of the nanoparticle to create the experimental setup to ensure the proper conditions required for our thesis research. We use this to create the basic water or buffer solution that our structure is within and later in the process this is used to simulate the different samples of biomolecules and their refractive indexes.

General

We go to "Simulation > Region > General". An option appears named "FDTD". We edit the object by setting the value of the "background index" to 1.33 to match the refractive index of water or a buffer solution. This ensures that the nanoparticle is completely immersed in water. Then, "Simulation Time" is set to 300 fs. As the simulation time increased to a larger value, the size of the file increases highly and it takes a very long time to obtain he results. On the other hand, if we set the simulation time to too much of a small value, we will not get the desired results. Hence, we have selected an optimum value of 300 fs.

Geometry

Now, we have selected the "Geometry" option located right next to "General". There are six options: x (nm), y (nm), z (nm), x span (nm), y span (nm) and z span (nm). The values of x and z are set to 0 and y to -26.2 which happens to be the origin point of our structure. This ensures that the simulation will occur over a range and not over a fixed value. That is why we use the x, y, z span options. The value of each span we are setting is 300, 400, 0 nm of x, y and z span respectively. This means that FDTD is automatically taking the nanorod couple as the center and there is a length of approximately 40 nm in 'y' direction around the rods.

Boundary Conditions

The boundary conditions that are supported by FDTD/MODE Solutions, which we have used for our research, are listed below. The values of "x min bc", "x max bc", "y min bc", "y max bc", "z min bc" and "z max bc" have been set to PML. The option "allow symmetry on all boundaries" have been unchecked. In the PML settings the "pml reflection" has been set to 0.0001. The applications and explanations of PML is listed below.

Perfectly Matched Layers (PML)

By construction, PML absorbing boundary conditions are impedance matched to the simulation region and its materials. This allows them to absorb light waves (both propagating and evanescent) with minimal reflection. An ideal PML boundary produces zero reflections, however, in practice there will always be small reflections due to the decentralization of the underlying PML equations. Furthermore, as a consequence of using finite difference approximations to decentralize the PML equations, there is some chance of producing numerical instabilities. The goal of this section is to outline best practices for minimizing reflection errors and getting rid of numerical instabilities without increasing simulation times unnecessarily.
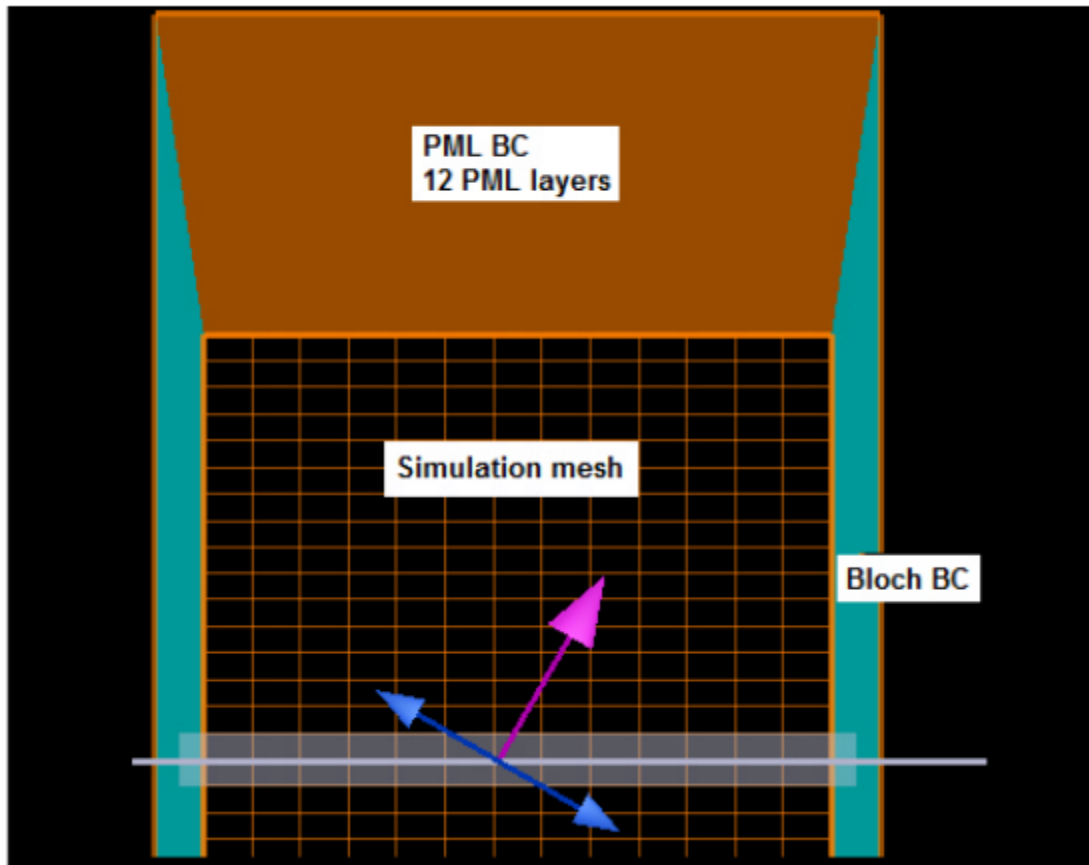
Figure 21 Schematic of PML

Mesh Analysis

After setting the conditions in FDTD, we can start with the mesh analysis. Accessibility of mesh is obtained from "Simulation > Mesh". The values of the "General" settings are set to 1 because lower values guarantee better accuracy. However, we do not take values less than 1, such as 0.5 or 0.25, because this increases the size of the file so much that the simulation time increases highly and after a few minutes into the simulation, the file shows an error and stops as our desktops did not have enough memory to support the computation. We can only use 0.5 of the mesh value to get a smooth and good quality result for electric filed, but not the entire simulation.

Figure 22 Applying mesh boundary

In this application, we use a combination of graded meshing and conformal meshing. The conformal meshing allows us to obtain more accurate results for a given mesh size. Even if the mesh size is only twice as large, for example 2 nm compared to 1 nm, the computation time in 3D simulations can be reduced by a factor of 16. We need to be careful when using conformal mesh technology with metals, however, and do some convergence testing to be sure that the conformal mesh technology is 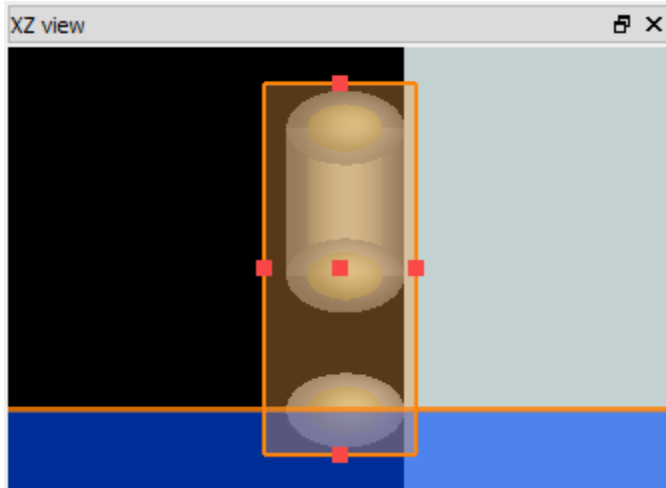appropriate for one's precise application.[24] Now, we select the mesh and go to its edit object. In the editing panel in "General" we override x, y and z mesh and set dx (nm) to 2. Afterwards, we proceed to the "Geometry" tab. In this tab just like most other geometry edits in this application we can set the origin point for our mesh with the x, y and z options while setting the width of each axis through its respective span. We set the origin point to (-15.25, -26.2, 0). Also the span is set to 50, 370 and 50 for x, y and z respectively. Later we will change the origin and the span to suite the variable lengths of the rods. These values will only be set as the baseline simulation. But in general we try to keep at least 5 nm gap between the rods and the mesh in each direction (x, y, z) around the particle.

Source

This is the light source that is being used to illuminate the entire experimental setup. With the purpose of adding a light source to our already existing apparatus, we follow "Sources > Total

Field Scattered Field (TFSF)". This installs the light source in the setup. Now, the object is edited to fit our testing.

In the "General" tab of the source we have an 'injection axis', this determines at which axis the light falls. We set this to the x-axis so it hits the nanorods and then the substrate. The direction is set to forward. Lastly, with all the phase and angles set to 0 we set the amplitude to 5. We move on the "Geometry" settings for our source. Once again the geometry is set up with origin point (x, y, z) and spans (x span, y span, z span). These settings for the light source are changed with variable lengths of the rods and the space in between them but always set so that they cover the whole structure and the mesh of the simulation. Lastly we have to deal with the last settings of "Frequency/Wavelength" tab. In this tab we can set either the frequency/wavelength range of the light or the time domain. At first we check the "override global source settings". Then we check the "set frequency/wavelength" box. This is done because we will be varying the wavelength range to get our results. In the "set frequency/wavelength" box we first choose wavelength and then a range between min and max. Wavelength start (nm) is set to 500 and the wavelength stop (nm) is set to 900. We predict our peaks and dip to be present within this range as we first set in to 200 to 1000 and got the initial graph. But such a long range wastes simulation time when our needed peaks and dips are situated in the 500 to 900 nm region.

Power Absorption (Advanced)

This is the advanced version of power absorption. Power absorption is taken into account so that we can observe the amount of power absorbed after the simulation is done in a graphical format. In order to access this feature, we go to "Analysis > Optical Power > Power absorbed (advanced)".

Once we go to edit the settings of this analysis we can see the various scripts that govern this analysis. This analysis returns the fraction of power from the source that is absorbed within the volume. The absorption is calculated using the following relation:
L=0.5*eps0*w*(abs(E))^2*imag(eps))

To provide a more accurate answer, the absorption is calculated from each field component

before doing the spatial interpolation to standard mesh cell locations. It outputs three things: Pabs, Pabs_total and f. Pabs is the power absorbed per unit volume at each position (x, y, z, f). Pabs_total is the total power absorbed within the monitor (f) and f is the simply the array of frequencies of light that the analysis is run against that comes from the source that we have set up previously.

Once again we have to set up the geometry region for the analysis to run. This geometry is also setup closely to the likes of the mesh geometry
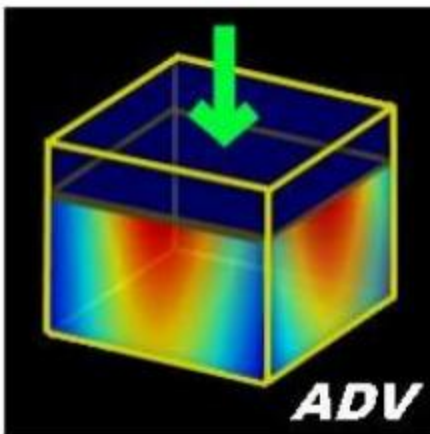
Figure 23 Pabs (Advanced) logo

Monitor

We went to "Monitor > Frequency – domain field and power". This object is then edited. The "override global monitor settings" is checked out. This allows us to enter the value of frequency points. We change the frequency points to "use source limits" an option inbuilt within the monitor.

Then we move on to the "Geometry". The Monitor Type is set to 2D X-normal (along the direction of the thickness of the substrate). X span automatically gets fixed to 0. If we fix the wavelength at a particular point rather than a range, Monitor gives us the electric filed or magnetic field pictures. We can even tweak the "Data to record" settings to select either electric field or magnetic field pictures or both if needed.

6.5 Summary

The software used in our simulation is FDTD Solutions by Lumerical. Lumerical develops photonic simulation software and tools. These tools help product designers to understand light, and predict how it behaves within complex circuits, structures and systems. Photonics is the study of light and its interaction with matter, and it unravels many opportunities for the world's leading technology companies across various fields including biotechnology, data communications, information storage, solar energy, environmental sensing and consumer electronics.

Among various products from Lumerical we have used the FDTD Solutions to simulate the structure and system we wanted to for our thesis. We have accurately designed our nanorods, its surroundings, substrate material, direction of incident light and electric field properties. The "Rounded Cylinder" option which was built-in helped us create our nanorods and also helped in varying the lengths, adjusting the material and its refractive index to our desired values. We used the "Rectangle" formation to create our Glass (SiO2) substrate that our nanorods will be sitting on. The FDTD options was used to set up the surroundings of our structure and simulate the different samples and analytes that the sensor chip had to be submerged in. Within this option we had to fix the geometry of the surroundings, the boundary conditions. As the light source the TFSF source was used and its direction of injection and wavelengths was varied within this option too. A mesh analysis region was set up so that the software knew which parts of this structure needed to be simulated and calculated for and the frequency of points in the 3D space it needed to do the Maxwell equation solving to get a smooth curve. Lastly, we set up a monitor and an analysis tool named Pabs (Advanced) in order to see our results of light power absorbed within the area while the monitor gave us the graphical representation of electric field.

7. Simulations and Results

7.1 Introduction

Once the structure and its surroundings were set up properly we begin to run the simulations while varying different variables we deemed necessary to get the most sensitive configuration of the structure. We also tested the baseline configuration through different refractive indexes to measure the sensitivity in respect to the primary peak and the dip in the Pabs curve. Lastly, we measured our most sensitive configuration on refractive indexes of different real life biomolecules found in the human body.

The results obtained from our simulations have been categorized into six parts:

- Ag coating thickness.
- Au coating thickness
- Nanorod position
- Substrate
- Sensitivity analysis using Peak and Fano Dip
- Sensitivity on Biomolecules.

First the method of getting a P_{abs} vs. Wavelength graph has to be described. Once the all the values have been set and the simulation finishes we get to visualize the graph from the Pabs (Advanced) analysis. Then the 300 points of data is taken into script and converted into a MATLAB file. The same is done for the frequency of incident light. In MATLAB the frequency is converted to wavelength and then graphed against the power absorbed array imported from FDTD Solutions.

7.2 Ag coating thickness

Here we used an Au (Gold) Nanorod with Ag (Silver) coating. Keeping the diameter of the Nanorod constant, we vary the thickness of the coating and the inner Au rod.

We can see that as the thickness of silver increases, the peaks become sharper. However, the dip flattens out. The profiles also shift to the left (blue-shift).

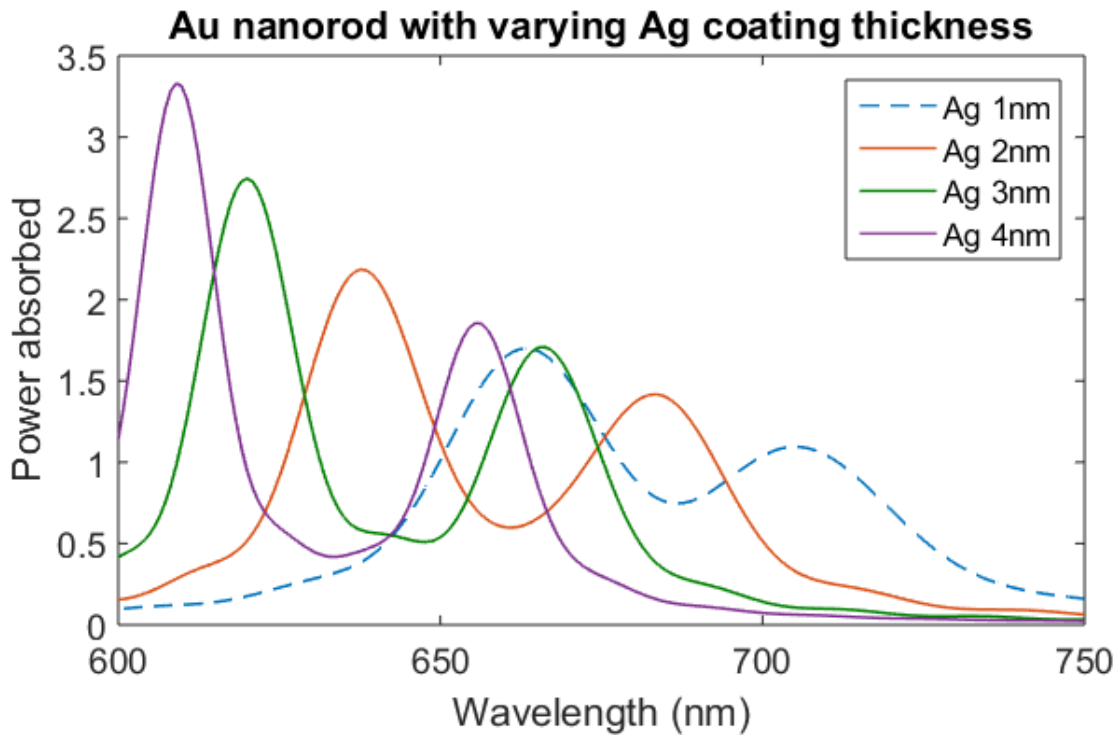| Thickness (nm)	Primary peak wavelength (nm)	Fano Dip wavelength (nm)	Secondary peak wavelength (nm)
1	663.2	686.6	705
2	637.7	661.2	683.5
3	620.0	647.8	666.2
4	609.0	633.1	655.4

Figure 24 Au nanorod with varying Ag coating thickness

7.3 Au coating thickness

Here we flipped the materials and made the Nanorod out of Ag (Silver) while keeping the coating material Au (Gold).

As before, we increased the thickness of gold coating while keeping the diameter of rod constant.

We can see that the peaks broaden and the overall Fano line-shape vanishes as we increase the coating thickness. The profiles also shift to the right (red-shift).

Since this configuration is not resilient to change, further simulations were carried out using Au Nanorod with Ag thicknesses of 1 or 2nm.

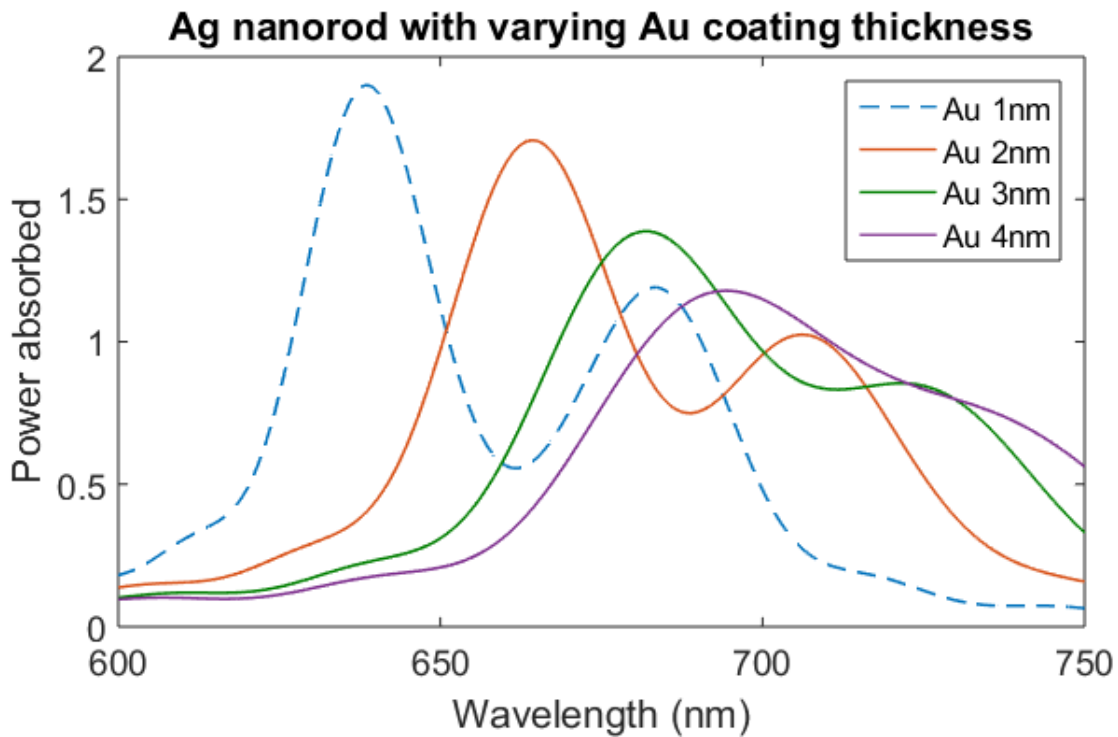| Thickness (nm)	Primary peak wavelength (nm)	Fano Dip wavelength (nm)	Secondary peak wavelength (nm)
1	638.6	661.2	683.5
2	664.2	688.8	706.2
3	681.8	711.8	721.0
4	694.6	N/A	N/A

Figure 25 Ag nanorod with varying Au coating thickness

7.4 Nanorod position

Au Nanorod with 1nm Ag coating used.

Here we changed the angle of the Nanorods with respect to each other. Initially, the rods were perpendicular to each other but an obtuse orientation does not produce Fano resonance.

We see a sharper LSPR peak (without any dips or secondary peaks) as we increase the angle from 120 through to 180 degrees where the rods are placed end to end.
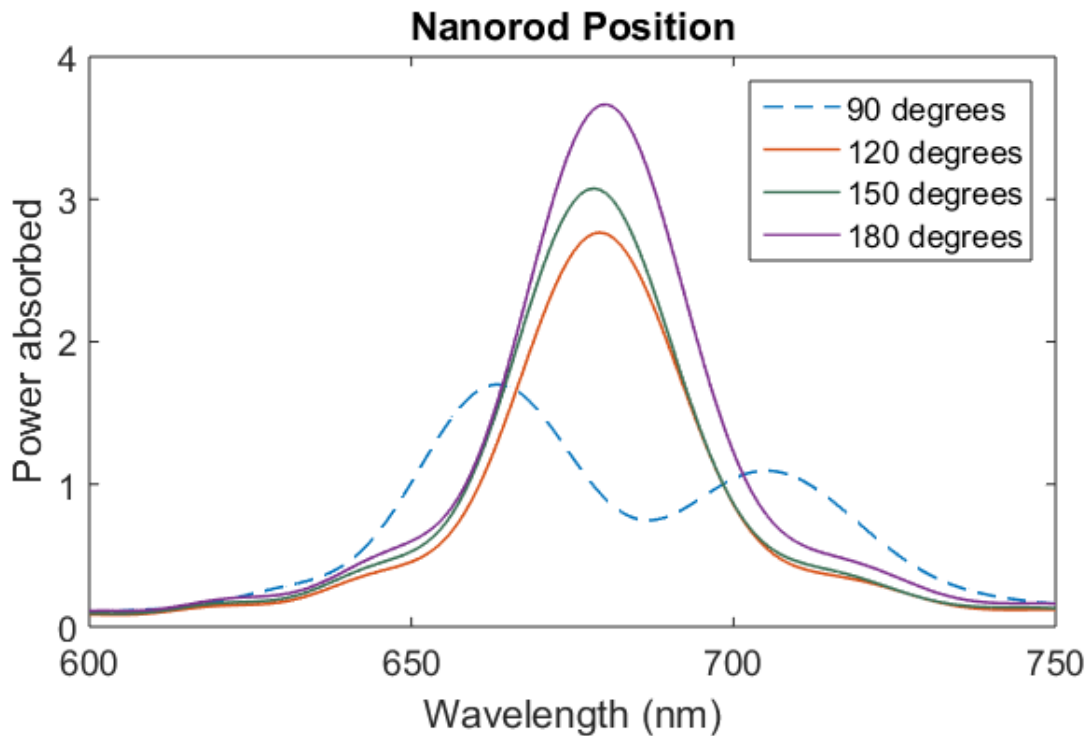
Figure 26 Nanorod position

7.5 Substrate

Au Nanorod with 2nm Ag coating used.

The substrate/dielectric (on which the Nanorods were placed) were changed to see whether a better response was found. We used alumina (Al2O3) and Indium-Tin-Oxide (ITO). Both of them return fano resonances but the response of glass (SiO2) is still better.

ITO is an expensive material used in touch-screen smartphones. Glass on the other hand is cheap and available.

Substrate	Primary Peak Wavelength (nm)	Fano Dip Wavelength (nm)	Secondary Peak Wavelength (nm)
SiO2 (Glass)	637.7	661.2	683.5
Al2O3 (Alumina)	666.2	687.7	708.4
ITO (Indium Tin Oxide)	664.2	684.5	702.8
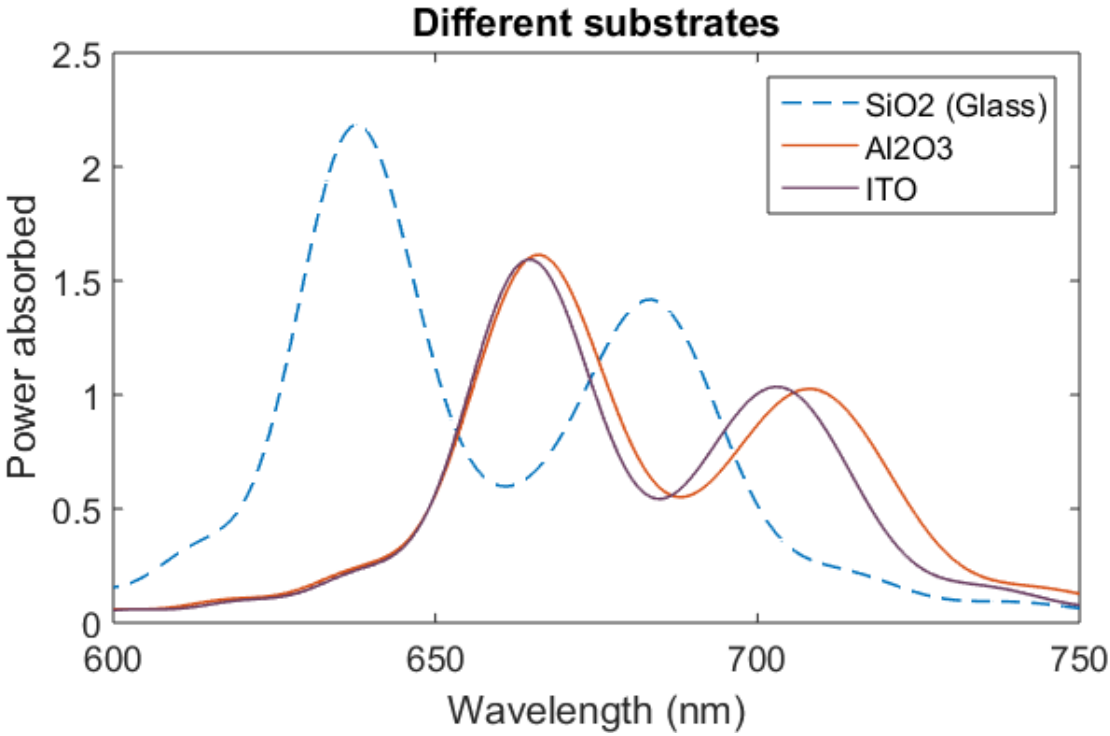
Figure 27 Effect of using different substrates

7.6 Sensitivity analysis

Au Nanorod with 1nm Ag coating used.

Our sensitivity analysis is performed by simulating changes in the refractive index of the surrounding medium. Starting point is taken to be water (1.33).

We can see that with each increment to the refractive index, the spectrum shifts to the right.

Refractive index	Primary Peak Wavelength (nm)	Fano Dip Wavelength (nm)	Secondary Peak Wavelength (nm)
1.33	663.2	686.6	705.0
1.38	676.2	699.5	718.6
1.40	681.4	706.2	724.5
1.42	686.6	710.7	730.4
1.45	694.1	719.8	738.2
1.50	707.3	732.8	750
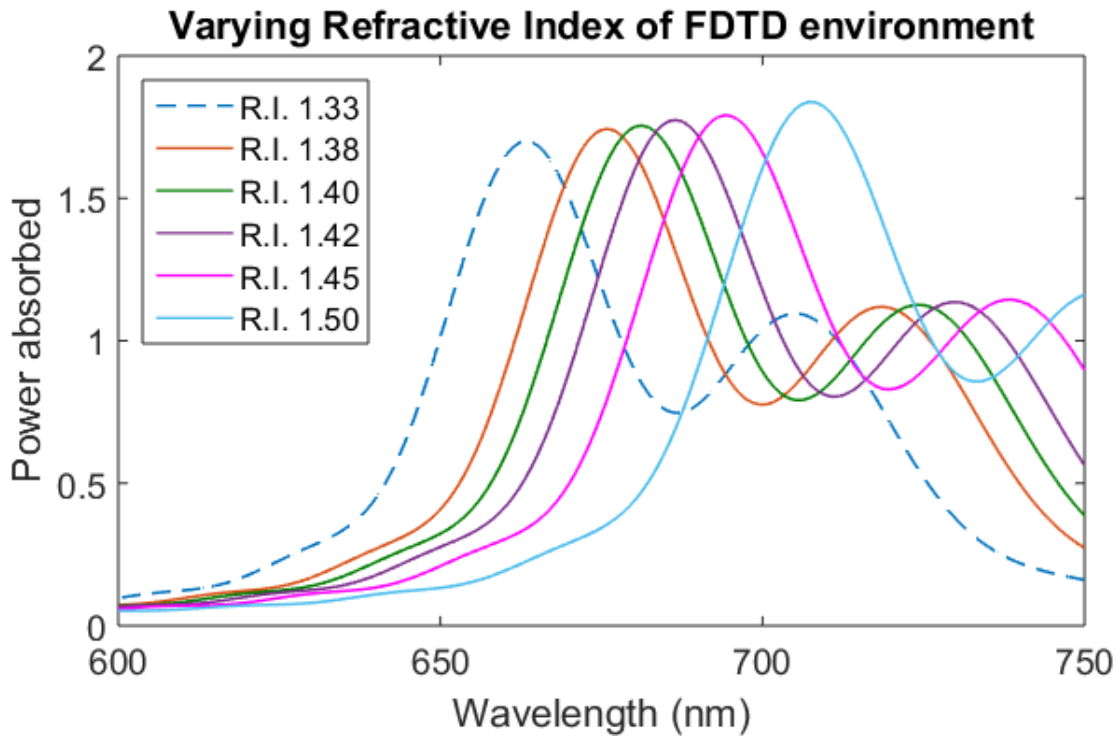
Figure 28 Varying refractive index of FDTD environment

Formula for sensitivity is shown here. We are going to calculate sensitivity for both the Primary Peak and the Fano Dip.

$$Sensitivity = \frac{d\lambda}{dn}$$

Where, dλ = Change in wavelength of incident light

dn = Change in refractive index

Tabulated form of primary peak shifts.

Refractive Index, n	Wavelength (nm) (λ)	SPR Shift (nm) (dλ)
1.33	663.2	00.0
1.38	676.2	13
1.40	681.4	18.2
1.42	686.6	23.4
1.45	694.1	30.9
1.50	707.3	44.1
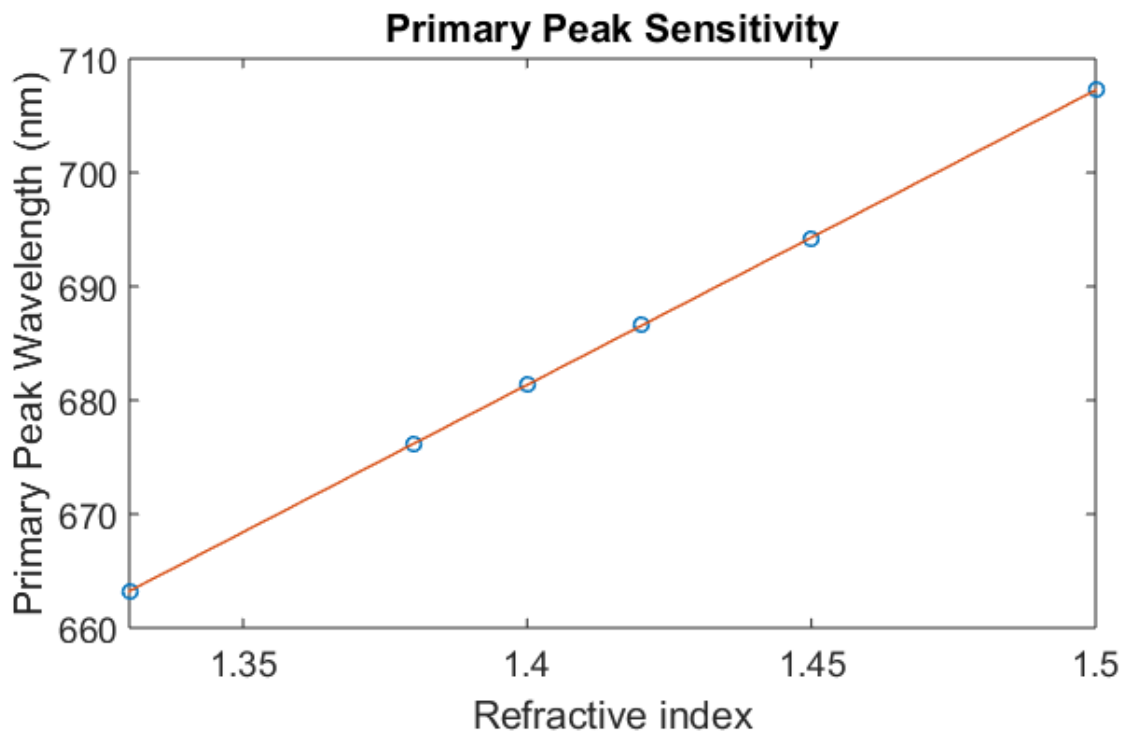
Figure 29 Primary peak sensitivity

- $Sensitivity = (686.53 - 676.17) \div (1.42\text{-}1.38) = 259$

- Line of best fit is drawn using the primary peak wavelengths. Slope of this line gives accurate sensitivity.

7.7 Fano dip

Similarly, the shifts in the fano dip are tabulated here.

Refractive Index, n	Wavelength (nm) (λ)	SPR Shift (nm) (dλ)
1.33	686.6	00.0
1.38	699.5	12.9
1.40	706.2	19.6
1.42	710.7	24.1
1.45	719.8	33.2
1.47	732.8	46.2
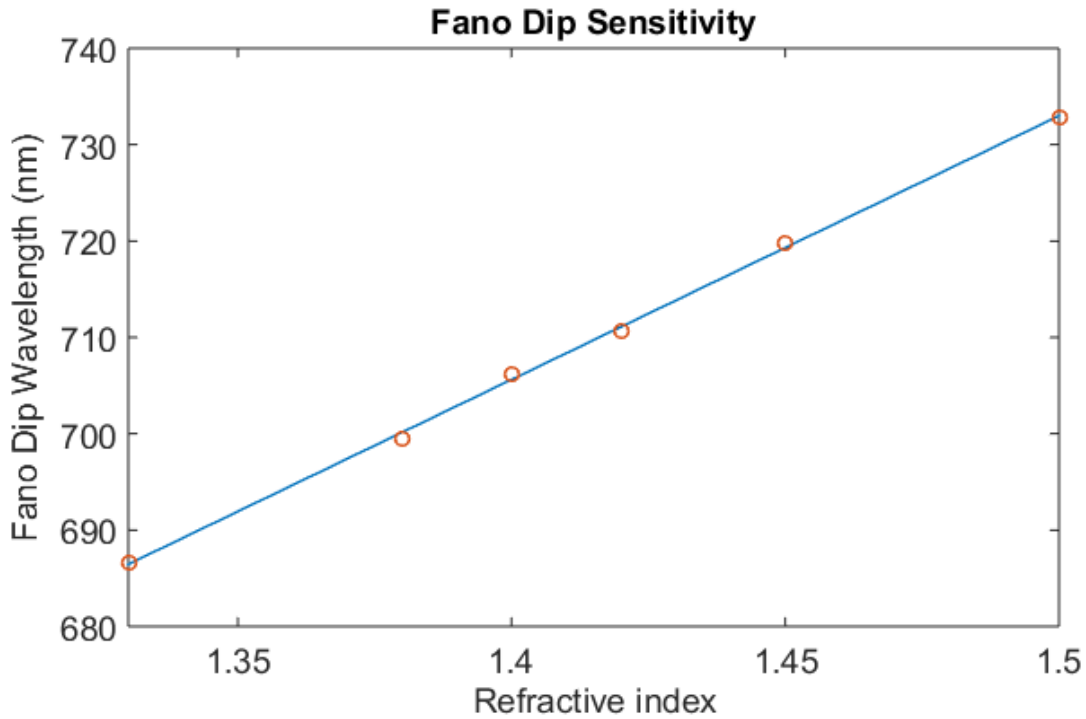
Figure 30 Fano dip sensitivity

- $Sensitivity = (711.09 - 700.14) \div (1.42-1.38) = 273.75$

- Similarly, we can run a sensitivity analysis using the dip. Sensitivity is also high here.

7.8 Sensitivity on Biomolecules

Recent data for individual biomolecules such as proteins or enzymes. Their corresponding refractive indexes are given.

Protein	Refractive Index	Primary Peak Wavelength (nm)	Fano Dip Wavelength (nm)	Secondary Peak Wavelength (nm)
Lys	1.495	637.7	660.3	682.4
HSA	1.445	634.9	661.2	683.5
Abn	1.45	638.6	663.2	684.5
CAT	1.465	641.3	666.2	687.7
Fb	1.39	639.5	662.2	683.0

Each one also has a different shape/size which also affects the shift in Fano resonance.
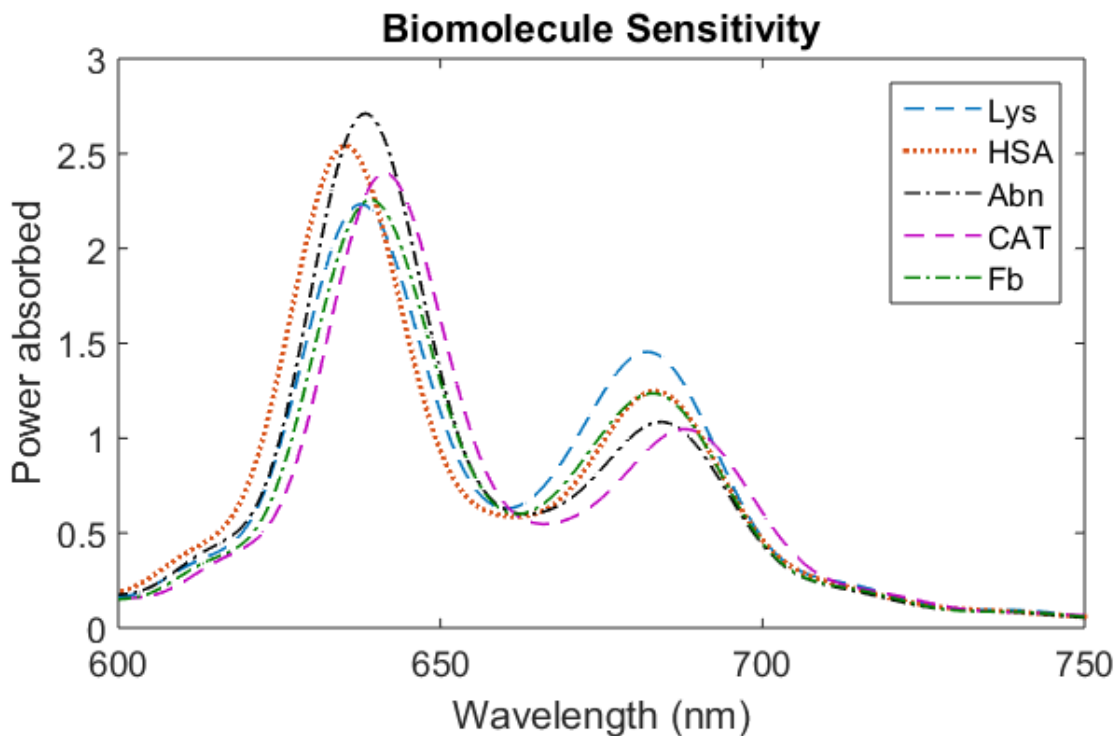
Figure 31 Biomolecule sensitivity

Primary peaks shifts are tabulated here.

Biomolecule	Wavelength (nm) (λ)	SPR Shift (nm) ($d\lambda$)
None (H$_2$O)	637.7	0.0
Lys	638.1	0.4
HSA	634.9	-2.8

Abn	638.6	0.9
CAT	641.3	3.6
Fb	639.5	1.8

Fano dip

Biomolecule	Wavelength (nm) (λ)	SPR Shift (nm) (dλ)
None	660.3	0.0
Lys	660.7	0.4
HSA	661.2	0.9
Abn	663.2	2.9
CAT	666.2	5.9
Fb	662.2	1.9

7.9 Summary

In this chapter, we have described the different variables we took from our structure and how we changed them to get better selectivity out of it. And at the end we discussed our results on the sensitivity analysis of our structure and the sensitivity it can show against real life biomolecules First the lengths of the Ag nanorod was changed into eight different values which gave us different shifts and changes in the primary peak and the fano dip and among those we chose the 200 nm length as the most sensitive configuration for its deep fano dip and highest primary peak Then we changed the length of the Al nanorod and it showed a broadening of the bandwidth of the secondary peak with the increase of the rod length. We chose the 152 nm length of the Al nanorod as the most sensitive configuration as a min-max of primary peak height and secondary peak bandwidth. We also changed the gap distance to show that as the gap increases the fano dip starts to rise and the fano resonance phenomenon decreasing. We also tested our structure through different refractive indexes to show the shift of the peaks and the dip as a proportional to the refractive index. From that we could also measure the sensitivity of the primary peak and the fano dip which showed the primary peak as the most sensitive detection method. Finally the sensor structure was tested against real data of four different proteins found in the human body. This test showed us a significant SPR shift which is very promising for detection from samples in real life scenarios. Overall, this chapter has proved the validity of our structure in terms of sensitivity and selectivity as a biomolecule detector.

8. Conclusion

8.1 Conclusion

This paper was done in the hopes of pursuing the unique characteristics of Localized Plasmon Resonance (LSPR) in colloidal nanoparticles. Besides its various applications in optics, photo catalysis, medicine and photovoltaic, we have seen its application in bio-sensing. The nanoparticle structure, comprised of a Silver nanorod and an Aluminum nanorod, placed closely together on a substrate (preferably Silicon Dioxide). The setup was immersed in water and illuminated with light. Our thesis research was based on the fanoresonance that occurred from the described setup and the fanodip found in the Absorption Cross-section curve. This fanoresonance can be widely tunable through a change in the different variables of the setup. We took Silver and Aluminum nanorod lengths, the gap between the rods. The length variable test was done by keeping one of the nanorods at a constant length while changing the length of the other one. At first the Silver nanorod length was taken as a variable and increased and decreased. A consistent rise in the height of the primary peak along with a broadening of the bandwidth of the secondary peak and fanodip is noticed. In this test the 200 nm length was chosen as the most sensitive configuration of the variable. The test with the Aluminum nanorod length was carried out similarly which showed a shortening bandwidth of the primary peak with increasing length. It also showed the fano dip getting shallower while the secondary peak getting wider with the increasing length. In this test the 152 nm length was chosen as the most sensitive configuration of the variable. We tested increasing the gap distance between the two nanorods from 10 nm to 30 nm. This test proved that the further away from each other the nanorods were placed the shallower the fano dip was getting. This shows that the nanorods had to be placed closely for fanoresonance to occur. Next, the sensitivity of the sensor structure was tested against an increasing refractive index starting from a base of 1.33 which represents water, all the way to 1.5 which represented biomolecules or proteins of heavy molecular density. This showed a proportionate increase in SPR shift with the increase of refractive index. This proves the validity of the structure as a bio detector. We found that the sensitivity of the primary peak was higher than that of the fano dip. Lastly the structure was faced against real data collected from proteins of the human body to see how much SPR shift we could expect in real life scenarios. The shifts in both the primary peak and the fano dip were significant enough to pass a selectivity test for each of the protein's detection.

In conclusion, optical properties of Al–Ag heterogeneous nanorod dimers are studied by theoretical simulation method. A pronounced Fano dip in the extinction spectra is observed, which strongly depends on both the geometry parameters of the complex nanostructure and the refractive index of the surrounding environment. The LSPR sensitivity of the heterogeneous metallic complex nanostructures is also checked and a sensitivity of 297.5 for the primary peak and 295 for the fano dip is obtained, which may find applications in biological sensing and molecule detection based on the coherent plasmonic coupling.

9. References

 [2] Chin, C. W., (2011). Localized Surface Plasmon Resonance with the use of Silver and Titanium Oxide Nanostructures. p. 1. Retrieved from:

http://web.utk.edu/~zzhang24/Chuck%20Chin%20Thesis.pdf

[3] Giannini, R. (1978). Shape Dependence of Localized Surface Plasmon Resonances and their application in nanoemmiters. Retrieved from:

http://e-collection.library.ethz.ch/eserv/eth:47630/eth-47630-02.pdf

[4] Stockman, M. I., (2011). Nanoplasmonics: the physics behind the applications. *Physics Today*, 39-44. Taken from:

http://physics.gsu.edu/stockman/data/Stockman_Phys_Today_2011_Physics_behind_Appl ications.pdf

[5] Maier, S. A. (2007) Localized Surface Plasmons. *Plasmonics: Fundamentals and applications*,p.65-72.

From:https://www.londonnano.com/sites/default/files/uploads/research/highlights/Nanoplasmonics/pdf

[6]*Plasmonics*

Retrieved from: https://www.physik.huberlin.de/de.nano/lehre/Gastvorlesung%20Wien/plasmonics

[7]*Surface Plasmon Resonance.*

Retrieved from:

https://en.wikipedia.org/wiki/Surface_plasmon_resonance

[8] Raether, H. (1988). Surface Plasmons on Smooth and Rough Surfaces and on Gratings. *Springer Tractsin ModernPhysics*, Vol. 111, Springer Berlin

[9] Localized Surface Plasmon Resonance Theory. *Localized Surface Plasmon Resonance vs. Surface Plasmon Resonance*. Retrieved from:

https://nicoyalife.com/technology/surfaceplasmonresonance/localized-surface-plasmon-resonance-theory/

[10] Free electron model (2016).

Retrieved from: https://en.wikipedia.org/wiki/Free_electron_model

[11] Biomolecule (2016).

Retrieved from: https://en.wikipedia.org/wiki/Biomolecule

[12] Lysozyme (2016).

Retrieved from: https://en.wikipedia.org/wiki/Lysozyme

[13] Human Serum Albumin (2016).

Retrieved from: https://en.wikipedia.org/wiki/Human_serum_albumin

[14] Immunoglobulin G (2016).

Retrieved from: https://en.wikipedia.org/wiki/Immunoglobulin_G

[15] About Lumerical. *lumerical*.

Retrieved from: https://www.lumerical.com/company/about_lumerical.html

[16] PDB-101: Lysozyme.

Retrieved from:

https://www.google.com/search?q=lysozyme&client=firefoxbab&source=lnms&tbm=isch&sa=

X&ved=0ahUKEwiy3oS81-

rQAhUBVhQKHf5eBJoQ_AUICSgC&biw=1366&bih=657#imgrc=J0_6P2nRKcicaM%3A

[17] Immunoglobulin G. Causes, symptoms, treatment Immunoglobulin G.

Retrieved from:

https://www.google.com/search?q=immunoglobulin+g&client=firefoxbab&source=lnms&tbm=i

sch&sa=X&ved=0ahUKEwia1KqJ2OrQAhVLthQKHca6D5cQ_

AUICCgB&biw=1366&bih=657#imgrc=3CSnlav6ZTO0eM%3A

[18] Entertainment - Home Page.

Retrieved from:

https://www.google.com/search?q=transmission+electron+microscope&client=firefoxbab&sourc

e=lnms&tbm=isch&sa=X&ved=0ahUKEwjq4sqK2erQAhVFXhQKHcpuBJUQ

_AUICCgB&biw=1366&bih=657#tbm=isch&q=transmission+electron+microscope+ima

ges+of+nanoparticles&imgrc=GioadFCbmkDLhM%3A

[20] Lumerical Solutions, Inc.

Retrieved from:

https://www.google.com/search?q=lumerical+solutions+logo&client=firefoxbab&source=lnms&

tbm=isch&sa=X&ved=0ahUKEwjmxIj54-

rQAhWFORoKHfhRBw4Q_AUICCgB&biw=1366&bih=657#imgrc=3iyJWdEBdavy3M%3A

[21] J. Fan, C. Wu, K. Bao, J. Bao, R. Bardhan, N. Halas, V. Manoharan, P. Nordlander, G. Shvets, F. Capasso (2010). Self-assembled plasmonic nanoparticle clusters. *Science*. 2010 May 28;328(5982):1135-8. doi: 10.1126/science.1187949.

Retrieved From:

https://www.ncbi.nlm.nih.gov/pubmed/20508125

[22] Periodic boundary conditions.

Retrieved from:

https://kb.lumerical.com/en/index.html?ref_sim_obj_symmetric_anti-symmetric.html

[23] Xueting Ci, Botao Wu, Min Song, Yan Liu, Gengxu Chen, E. Wu, Heping Zeng. Tunable Fano resonances in heterogenous Al–Ag nanorod dimers. *Appl. Phys A*. doi: 10.1007/s00339-014-8479-z

[24] Mesh refinement.

Retrieved from:

https://kb.lumerical.com/en/index.html?ref_sim_obj_symmetric_anti-symmetric.html

[25] Wilson, W. L., Szajowski, P. F. & Brus, L. E. (1993). Quantum confinement in sizeselected surface-oxidized silicon nanocrystals. *Science* 262, 1242-1244.

[53] Ming, T., Zhao, L., Yang, Z., Chen, H., Sun, L., Wang, J. & Yan, C. (2009). Strong polarization dependence of plasmon-enhanced fluorescence on single gold nanorods. *Nano Lett*. 9, 3896-3903.

[54] Thompson, P. G., Biris, C. G., Osley, E. J., Gaathon, O., Osgood Jr., R. M., Panoiu, N. C. & Warburton, P. A. (2011). Polarization-induced tunability of localized surface plasmon resonances in arrays of sub-wavelength cruciform apertures. *Opt. Express* 19, 25035- 25047.

[55] Kooij, E. S. & Poelsema, B. (2006). Shape and size effects in the optical properties of metallic nanorods. *Phys, Chem. Chem. Phys*. 8, 3349-3357.

[56] Kooij, E. S., Ahmed, W., Zandvliet, H. J. W. & Poelsema, B. (2011). Localized surface plasmons in noble metal nanospheroids. *J. Phys. Chem*. C 115, 10321-10332.

[57] Sönnichsen, C., Franzi, T., Wilk, T., von Plessen, G & Feldmann, J. (2002). Drastic reduction of plasmon damping in gold nanorods. Phys, Rev. Lett. 88, 077402.

[58] Zoric, I., Zach, M., Kasemo, B., & Langhammer, C. (2011). Material independence, subradiance, and damping mechanisms. *ACS Nano* 5, 2535-2546.

[59] Sönnichsen, C., Franzl, T., von Plessen, G. & Feldmann, J. (2002). Plasmon resonances in large noble-metals clusters. *New Journal of Physics* 4, 93. 1-93.8.

[60] (2000). Light scattering by nonspherical particles. Edited by Mishchenko, M. I., Hovenier, J. W. & Travis, L. D., Academic Press.

[61] Novotny, L. & Brecht, B. (2006). Principles of nano-optics. University Press, Cambridge.

[62] Hohenester, U. & Krenn, J., (2005). Surface plasmon resonances of single and coupled metallic nanoparticles: A boundary integral method approach. *Phys. Rev. B* 72, 195429.

[63] Berkovitch, N., Ginzburg, P. & Orenstein, M. (2012). Nano-plasmonic antennas in the near infrared regime. *J. Phys.: Condens. Matter* 24, 073202.

[64] Mock, J. J., Barbic, M., Smith, D. R., Schultz, D. A. & Schultz, S. (2002). Shape effects in plasmon resonance of individual colloidal silver nanoparticles. *J. Chem. Phys*. 116, 6755-6759

[65] Bryant, G. W. (2008). Mapping the plasmon resonances of metallic nanoantennas. *Nano Lett*.8, 631-363.

[66] Boris luk'yanchuk1, Nikolay I. Zheludev, Stefan A. Maier, Naomi J. Halas, Peter Nordlander, Harald Giessen and Chong Tow Chong. The Fano resonance in plasmonic nanostructures and Metamaterials. *Nature Materials.* Published online: 23 August 2010. doi: 10.1038/nmat2810

[67]Fibrinogen.